CANCER

Cell-cell communication network-based interpretable machine learning predicts cancer patient response to immune checkpoint inhibitors

Juhun Lee[1]†, Donghyo Kim[1], JungHo Kong[1], Doyeon Ha[1], Inhae Kim[2], Minhyuk Park[1], Kwanghwan Lee[1], Sin-Hyeog Im[1,2,3], Sanguk Kim[1,3]*

Immune checkpoint inhibitors (ICIs) have revolutionized cancer treatment. However, only some patients respond to ICIs, and current biomarkers for ICI efficacy have limited performance. Here, we devised an interpretable machine learning (ML) model trained using patient-specific cell-cell communication networks (CCNs) decoded from the patient's bulk tumor transcriptome. The model could (i) predict ICI efficacy for patients across four cancer types (median AUROC: 0.79) and (ii) identify key communication pathways with crucial players responsible for patient response or resistance to ICIs by analyzing more than 700 ICI-treated patient samples from 11 cohorts. The model prioritized chemotaxis communication of immune-related cells and growth factor communication of structural cells as the key biological processes underlying response and resistance to ICIs, respectively. We confirmed the key communication pathways and players at the single-cell level in patients with melanoma. Our network-based ML approach can be used to expand ICIs' clinical benefits in cancer patients.

INTRODUCTION

Immune checkpoint inhibitors (ICIs) have revolutionized cancer treatment. ICIs provide durable clinical benefits to patients with advanced-stage cancer (*1*). ICI-based therapeutic strategies are being extended to many cancer types, such as lung cancer, bladder cancer (BC), gastric cancer (GC), and melanoma (*1*, *2*). However, only a small proportion of patients with cancer benefit from ICI-based therapy due to low response rates (*1*, *2*). ICIs boost antitumor immunity to eliminate tumors by interfering with the interactions between immune checkpoint molecules of the cells in the tumor immune microenvironment (TIME) (*3*). Distinct immunological characteristics of the TIME in each patient brought about heterogeneous ICI efficacy. Thus, a method to predict patient response to ICIs based on the key biological processes of the TIME is necessary to ensure its clinical benefits.

Various biomarkers of ICI efficacy have been investigated to classify patients as responders (R) and nonresponders (NR). However, these biomarkers do not take cell-cell communication into account. Cell-cell communication shapes patient-specific immunological characteristics because they control immune cell activities (*4*). For example, $CD8^+$ T cells play an essential role in tumor elimination, but their levels do not correlate with ICI efficacy (*5*, *6*). The levels of $CD8^+$ T cells entailed dysfunctional or exclusive states of T cells that are incapable of eliminating tumors (*6*). Neighboring cells of $CD8^+$ T cells, including myeloid-derived suppressor cells, tumor-associated macrophages (TAMs), and cancer-associated fibroblasts (CAFs), induce these states through cytokines or cell-cell contact (*7*, *8*). Programmed cell death ligand 1 (PD-L1) levels have been used to predict ICI efficacy because the interaction between PD-L1 in tumor cells and programmed cell death 1 (PD1) of T cells induces immune evasion (*9*). However, previous studies have reported that PD-L1 levels exhibit a limited correlation with ICI efficacy (*10*–*12*). In addition to PD-L1 and PD1 interaction, interleukin-10 (IL-10) or transforming growth factor–β (TGF-β) secreted from regulatory T cells (T_{regs}) also mediates immune evasion by suppressing effector T cell activity (*13*).

We hypothesized that (i) cell-cell communication networks (CCNs) can predict patient response to ICIs and (ii) identify key communication pathways involving key players for the prediction of ICI efficacy. A CCN, composed of cell types as nodes and communication strength between two cells as links, describes cell-to-cell regulatory relationships that organize an antitumor immune response in the TIME. For example, melanoma cells repress cytotoxic T cells by CAFs via the secretion of IL-1a or IL-1b (*14*). In contrast, the activation of $CD8^+$ T cells requires sequential communication of antigen priming, costimulation, and cytokine signaling mediated by antigen-presenting cells (APCs) to eliminate tumors (*15*). B cells activate T cells via cell-cell contact (*16*). They form a tertiary lymphoid structure (TLS) by recruiting immune cells using chemokines, which is important for antitumor immunity (*16*).

Recent development in single-cell technology has enabled us to construct patient-specific CCN. CCNs for each patient are based on the patient's bulk tumor transcriptome that encodes the gene expression profiles of tumors and neighboring cells. The bulk transcriptome data were dissected into cell type–specific gene expression profiles (*17*). The communication strength between two cells was measured using the cell type–specific gene expression levels of ligands, receptors, and cofactors (*18*).

The CCN elucidates key communication pathways involving the key players responsible for ICI efficacy when incorporated with an interpretable machine learning (ML)–based approach. The ML model trained using CCN to predict patient responses to ICIs learned critical cell-cell communications for ICI efficacy. The interpretation of the ML model revealed which communication pathways and players led to a response or nonresponse. Previously, network-based ML approaches were adopted to identify key players and biological pathways in diverse systems. For example, network-based approaches have been applied to identify key players in criminal, social, and infrastructure networks (*19*). Moreover, network-based ML approaches have successfully identified important biological pathways, such as

[1]Department of Life Sciences, Pohang University of Science and Technology, Pohang 790-784, Korea. [2]ImmunoBiome Inc., Pohang 166-20, Korea. [3]Institute of Convergence Science, Yonsei University, Seoul 120-749, Korea.
*Corresponding author. Email: sukim@postech.ac.kr
†Present address: ImmunoBiome Inc. Pohang 166-20, Korea.

the activation of BH3-only proteins or antigen presentation for the response of chemotherapy and immunotherapy, respectively (*20*, *21*). These approaches can help establish ICI-based combinatorial therapeutic strategies. For example, targeted inhibitors in combination with ICIs overcome resistance to ICI by suppressing key communication pathways with key players for the resistance (*22*, *23*).

Here, we constructed a CCN for each patient by decoding the bulk tumor transcriptome of the patient and found that the interpretable ML model using CCNs could predict patient response to ICI therapies across four cancer types (melanoma, lung, bladder, and gastric cancers). Furthermore, the CCN-based ML model revealed key communication pathways and players responsible for ICI response and resistance. We validated our framework by analyzing data for >700 ICI-treated patient samples from 11 cohorts. Chemotaxis-mediated communication pathway of immune-related cells was found to be the key pathway for response to ICIs. In contrast, growth factor–mediated communication of structural cells mainly participated in resistance to ICIs. Notably, in melanoma, the key processes, as per the CCN-based ML model, were confirmed at the single-cell level. Last, the genes involved in the key communication pathways prioritized for resistance to ICIs were identified as the potential drug targets for ICI-based combinatorial therapies.

RESULTS

CCN-based interpretable ML models predict patient response and identify key communication pathways with cells to ICIs

CCNs were constructed using the following two steps: (i) deconvolution of the bulk tumor transcriptome of patients into cell type–specific gene expression profiles and (ii) measurement of communication strength between the cells. The deconvolution was based on the signature gene expression of a cell type (*17*) and was performed for the following four cancer types: melanoma, non–small cell lung cancer (NSCLC), GC, and BC (Fig. 1A, fig. S1, Materials and Methods). The communication strength between the cells, called communication probabilities, were measured using gene expression levels of ligands, receptors, and cofactors of each cell type (*18*) (Fig. 1A, fig. S1, Materials and Methods). A cell expressing ligand was denoted as the source cell, and a cell expressing receptor was denoted as the target cell. The communication probabilities of ligand-receptor pairs with similar biological functions were integrated into a specific communication pathway.

The CCN-based interpretable ML model was trained using communication probabilities, which contained information regarding molecular function, source cells, and target cells. In contrast, the gene-based ML models were trained using the gene expression levels (Fig. 1B). CCN-based ML models takes the key interactions between source and target cells in the tumor microenvironment to predict responsiveness to ICIs, leading to better predictive performance of patient response to ICI treatment and the identification of key communication pathways, source cells, and target cells.

CCN-based ML model outperforms gene-based ML models

The predictive performance of CCN-based ML models was superior to that of gene-based ML models for patient response to ICIs across the four cancer types (Fig. 2). First, the construction of CCN was responsible for the improvement in the prediction of cancer patient response to ICIs (Fig. 2, A to I, and fig. S2, A to G). The predictive performance of the CCN-based ML model was compared with that of the ML model trained using gene expression data used for CCN construction (Fig. 2A). The CCN-based ML model exhibited significantly higher predictive performance [median area under the receiver operating characteristic curve (AUROC): 0.79] across seven independent cohorts [four melanoma cohorts; VanAllen *et al.* (*24*), Liu *et al.* (*25*), Gide *et al.* (*26*), Hugo *et al.* (*27*), a NSCLC cohort; Jung *et al.* (*28*), a BC cohort; Mariathasan *et al.* (*29*), a GC cohort; Kim *et al.* (*30*)] than that trained without CCN (Fig. 2, B to I, and fig. S2, A to G; two-sided Wilcoxon signed-rank test; $P < 0.05$ was considered significant).

Next, The CCN-based ML model exhibited significantly higher predictive performance for patient response to ICIs than other ML models based on previously used ICI biomarkers (Fig. 2, J to Q, and fig. S2, H to O; two-sided Wilcoxon signed-rank test; $P < 0.05$ was considered significant). For these ML models, the expression levels of ICI target genes, TIME-associated genes, and cellular proportions inferred by the deconvolution were used (*6*, *31*) for comparison (Materials and Methods).

We found that biologically relevant relationships among ligands, receptors, and cofactors were key to the improved performance of the CCN-based ML model (fig. S3). We compared the predictive performances of the CCN-based ML models with those trained using randomized CCNs constructed by randomized ligand, receptor, and cofactor relationships (randomized L/R CCN) (fig. S3A). The predictive performance of the randomized L/R CCN–based ML model was poor, suggesting that appropriate relationships among communication molecules were important for improved prediction of patient response to ICIs (fig. S3, B to P; two-sided Wilcoxon signed-rank test; $P < 0.05$ was considered significant).

Moreover, we found that cancer type–specific CCN was essential for the predictive performances of CCN-based ML models. The predictive performances of cancer type–specific CCN-based ML models were superior to those of cancer-type nonspecific CCN-based ML model with statistical significance, suggesting that construction of cancer type–specific CCN was important for the performances of CCN-based ML models (fig. S4; two-sided Mann-Whitney *U* rank test; $P < 0.05$ was considered significant).

CCN-based ML model identifies CXCL-sending and CXCL-receiving CD8$^+$ T cells as key factors for patient response to ICIs in melanoma

To expand the clinical benefits of ICI treatment for patients with cancer, it is important to identify the mode of action responsible for patient response or resistance to ICIs. Regarding patient response to ICIs, we found chemotaxis-mediated communications of immune-related cells to be the key biological process (Figs. 3 to 5).

Specifically, CXCL-sending and CXCL-receiving CD8$^+$ T cells were identified as the key players behind patient response to ICIs in melanoma (Fig. 3). To identify the key communication pathway, the pathway importance score (PIS) was defined as the summation of all feature importance in each communication pathway (Fig. 3A). The higher the PIS, the more associated the pathway was with R (i.e., response to ICIs), whereas the lower the PIS, the more associated the pathway was with NR (i.e., resistance to ICIs) (Fig. 3A).

We found that the PIS was correlated with patient response to ICIs (Fig. 3B and fig. S5). The higher score exhibited better average predictive performance of the top N pathways in the independent cohort (Fig. 3B and fig. S5). To validate the relevance between PIS and patient

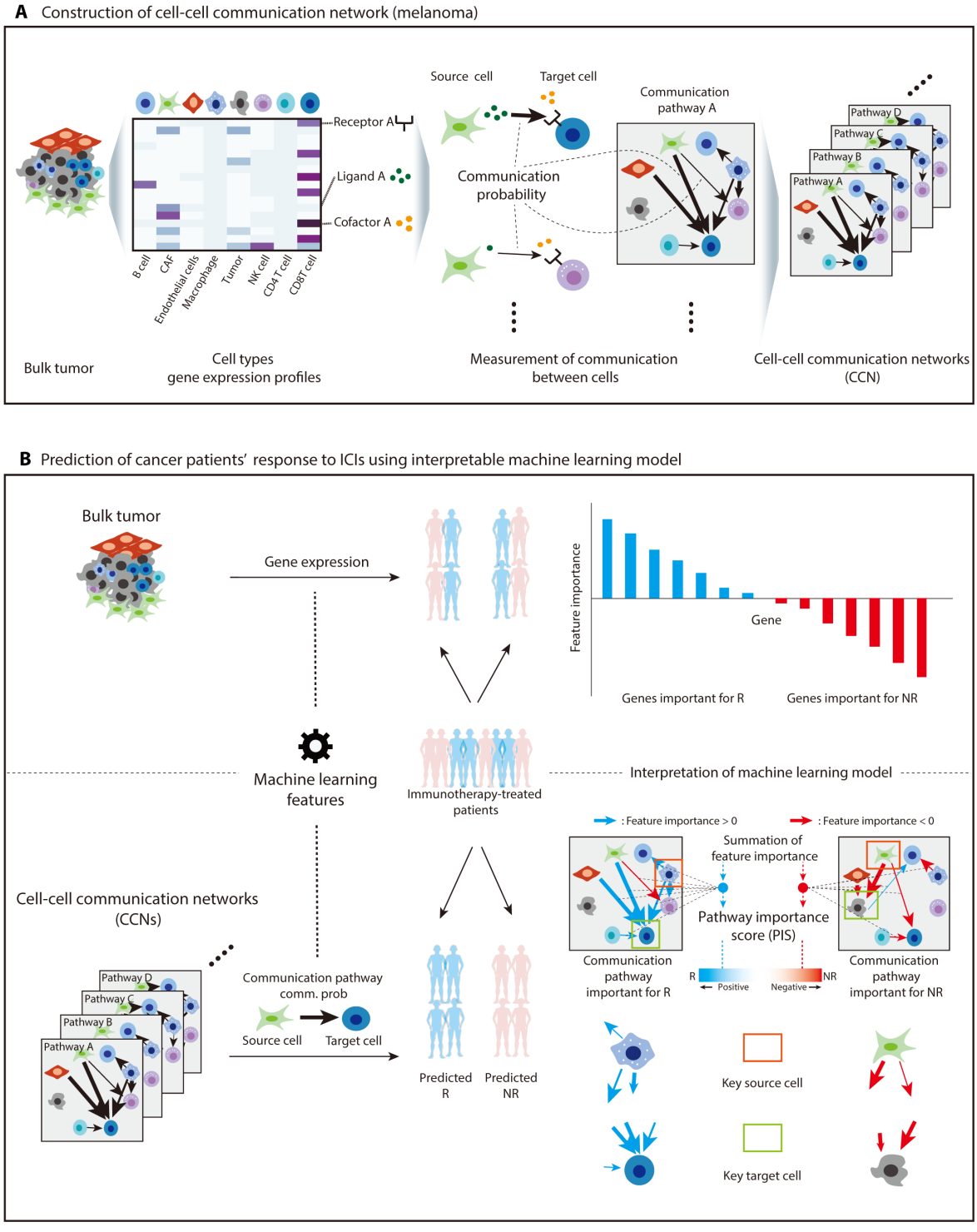

Fig. 1. Overview of CCN-based interpretable ML model to predict response of cancer patients to ICIs. (**A**) Construction of CCN for melanoma. Bulk tumor transcriptome data of patients were deconvoluted into cell type–specific gene expression profiles. Expression levels of ligands, receptors, and cofactors in each cell type were used to measure the communication probability between two cells i.e., the communication strength between a source cell and a target cell, was calculated. Communication probabilities calculated by ligands, receptors, and cofactors having similar biological functions were integrated into a specific communication pathway. CCN was constructed on the basis of the communication probabilities across all communication pathways using bulk tumor transcriptome data of a patient. (**B**) CCN-based ML model exhibited better prediction of patient response to ICIs than the gene expression-based ML model, in terms of predictive performance and interpretability. CCN-based ML model was trained using communication probabilities, which had information about the function, source cell, and target cell of the communication pathway. The interpretation of the ML model can identify a key communication pathway, source cell, and target cell for response or resistance to ICIs.

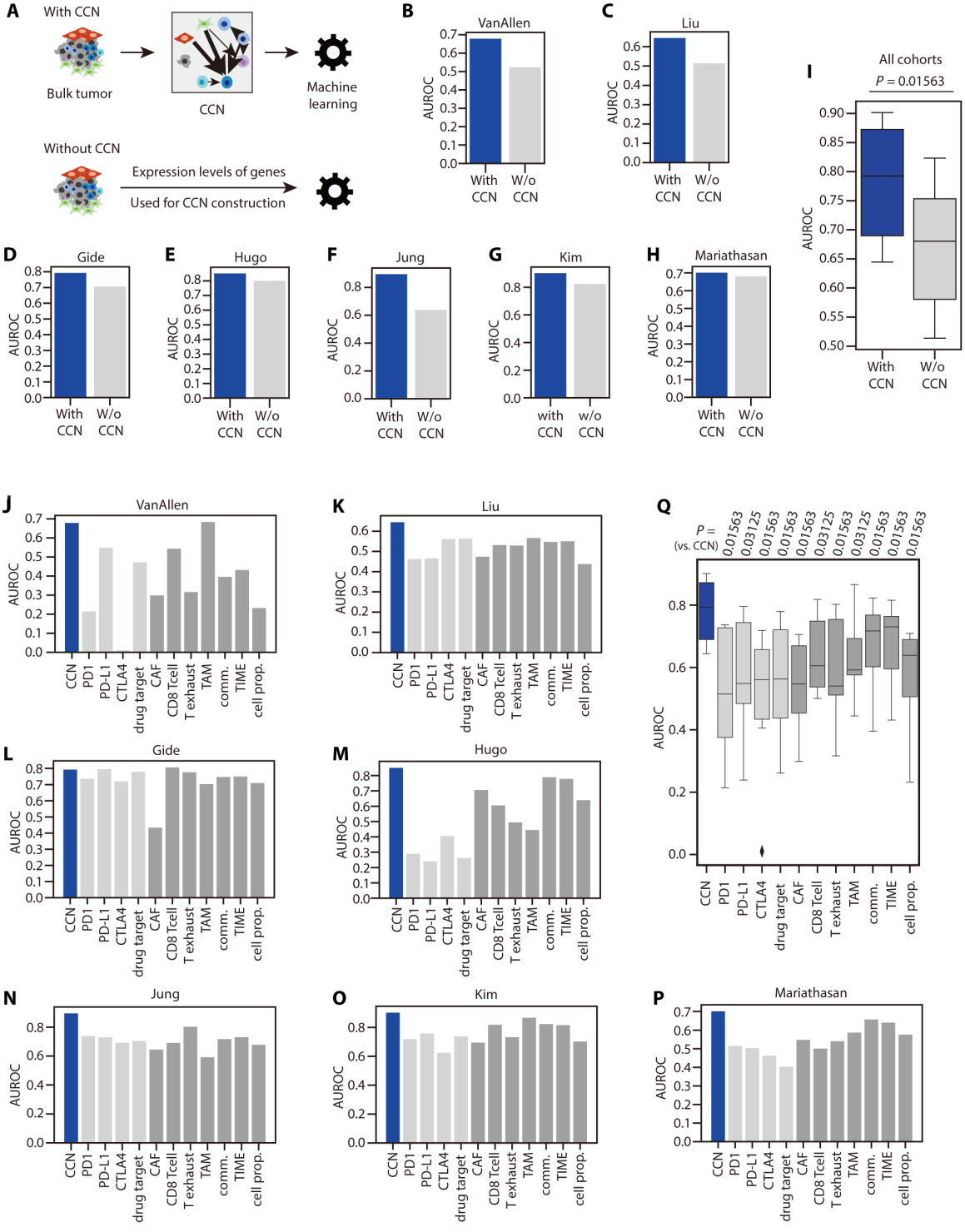

Fig. 2. Predictive performances of CCN-based ML models in seven independent ICI-treated cohorts. (**A**) A concept describing the comparison between the CCN-based ML model (denoted as "with CCN") and the ML model "without CCN." The without CCN model was trained using the expression levels of ligands, receptors, and cofactors used for constructing CCN. (**B** to **H**) Predictive performances of the CCN-based ML model compared with those of the model without CCN. (**I**) Comparison between the CCN-based ML model and the model without CCN across all cohorts. (**J** to **P**) Predictive performances of the CCN-based ML model compared with those of the models trained using ICI-related biomarkers. (**Q**) Comparison of the CCN-based ML model with the models trained using ICI-related biomarkers across all cohorts. Predictive performances shown in the [(B) and (J)] VanAllen, [(C) and (K)] Liu, [(D) and (L)] Gide, [(E) and (M)] Hugo, [(F) and (N)] Jung, [(G) and (O)] Kim [(H) and (P)], and Mariathasan cohorts were assessed by calculating the AUROC curve after conducting a leave-one-out cross-validation (LOOCV). Statistical significance of (I) and (Q) was calculated using the two-sided Wilcoxon signed-rank test. Each datapoint of boxplots in (I) and (Q) indicates the AUROC measured in each cohort. Boxplots of (I) and (Q) show median value, interquartile range (IQR) as bounds of the box, and whiskers that extend from the box to upper/lower quartile ± IQR × 1.5.

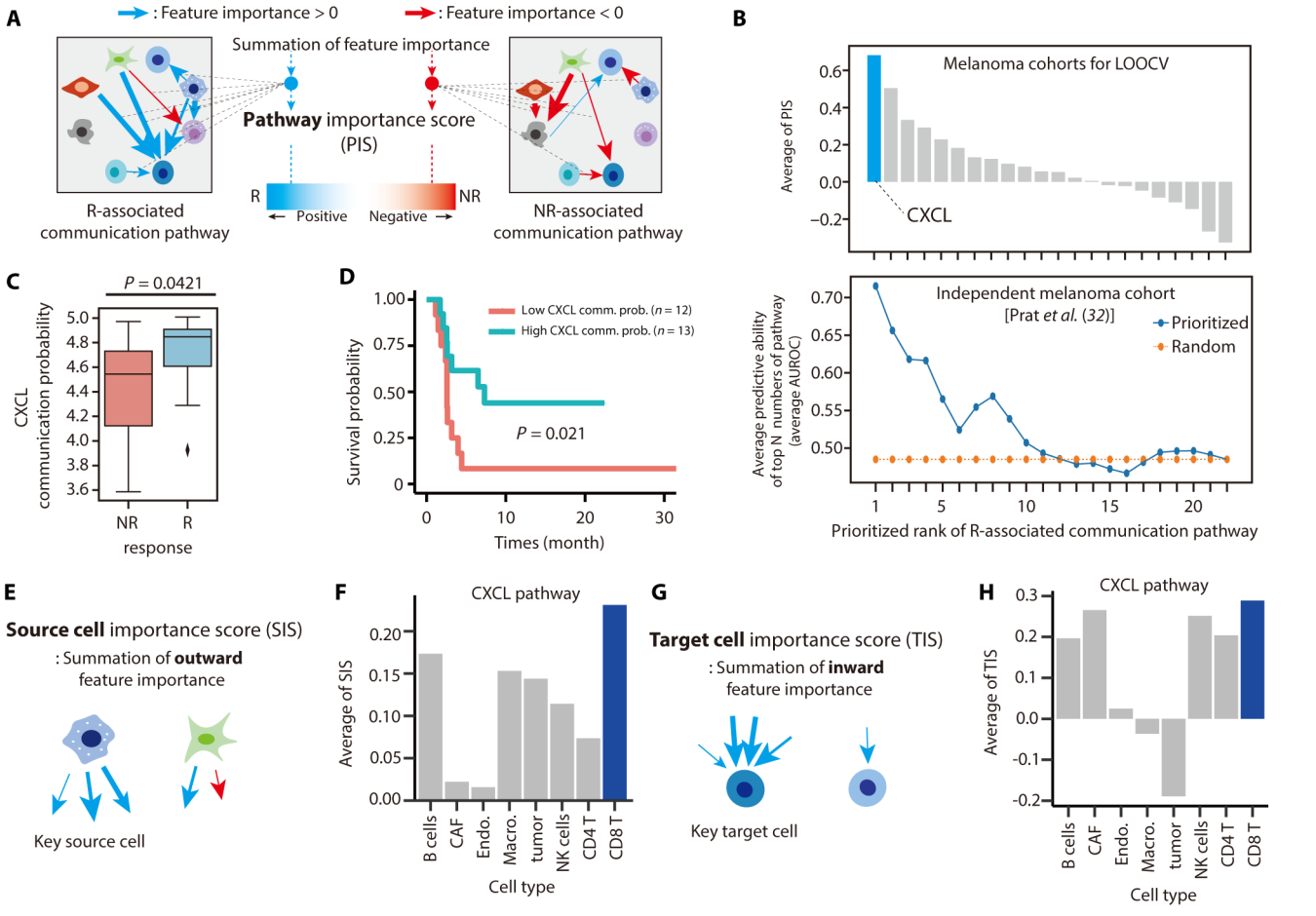

Fig. 3. Association of CXCL communication–sending and CXCL communication–receiving CD8$^+$ T cells with patient response to ICIs based on the interpretation of the CCN-based ML model in melanoma. (**A**) Definition of PIS (Materials and Methods). The higher the PIS, the more likely the association of the communication pathway with responders (i.e., response to ICIs), whereas, the lower the PIS, the more likely the association of the pathway with nonresponders (i.e. resistance to ICIs). (**B**) Prioritization of a key communication pathway by PIS and association of the prioritized pathway with patient response to ICIs in an independent ICI-treated melanoma cohort (*32*). (**C** and **D**) Association of CXCL communication with (C) response to ICIs and (D) PFS in an independent ICI-treated melanoma cohort (*32*). Statistical significance of (C) and (D) was calculated using the two-sided Mann-Whitney *U* rank test and the two-sided log-rank test, respectively. Boxplot shows median value, IQR as bounds of the box, and whiskers that extend from the box to upper/lower quartile ± IQR × 1.5. (**E**) Definition of SIS (Materials and Methods). (**F**) Identification of the key source cell in the CXCL communication pathway by an average of the SIS across four melanoma cohorts. (**G**) Definition of TIS (Materials and Methods). (**H**) Identification of the key target cell in the CXCL communication by an average of the TIS across four melanoma cohorts. The key source cell and the key target cell were designated as the cells with the highest SIS and TIS, respectively. Abbreviation of cell types shown in (F) and (H): cancer associated fibroblast, CAF; endothelial cell, Endo.; macrophages, Macro.; CD4$^+$ T cells, CD4 T; and CD8$^+$ T cells, CD8 T.

response to ICIs, we used an ICI-treated melanoma cohort of (*32*) as the independent cohort. The pathways were then sequentially arranged by average PIS, and the average predictive performance of the top N pathways was measured in the independent cohort.

The CCN-based ML model identified CXCL communication as the key pathway for response to ICIs in melanoma. CXCL exhibited the highest average PIS and was consistently associated with R in all melanoma cohorts (Fig. 3B and fig. S6). To validate that CXCL was associated with response to ICIs, we tested whether CXCL communication probabilities could differentiate the clinical outcomes of melanoma patients treated with ICIs using the independent cohort. The CXCL communication probability of R was significantly higher than that of NR (Fig. 3C), and patients with high CXCL probabilities exhibited better progression-free survival (PFS) than those with low CXCL probabilities (Fig. 3D).

Next, the CCN-based ML model identified CD8$^+$ T cells as the key source and target cell of the CXCL pathway for patient response to ICIs. We defined source cell importance score (SIS) and target cell importance score (TIS) to identify the key players behind patient response to ICIs. SIS was calculated by a summation of outward feature importance, and the cell type with the highest SIS was assigned as a key source cell (Fig. 3E). CD8T cells exhibited the highest average SIS across the four melanoma cohorts (Fig. 3F). Meanwhile, TIS was measured by a summation of the inward feature importance. The cell type with the highest TIS was assigned as the key target cell (Fig. 3G). CD8$^+$ T cells exhibited the highest average TIS (Fig. 3H).

We validated that CXCL-sending and CXCL-receiving CD8$^+$ T cells were associated with patient response to ICIs at the single-cell level in melanoma (Fig. 4). We investigated whether CD8$^+$ T cell subtypes overexpressing both CXCL ligands and receptors were

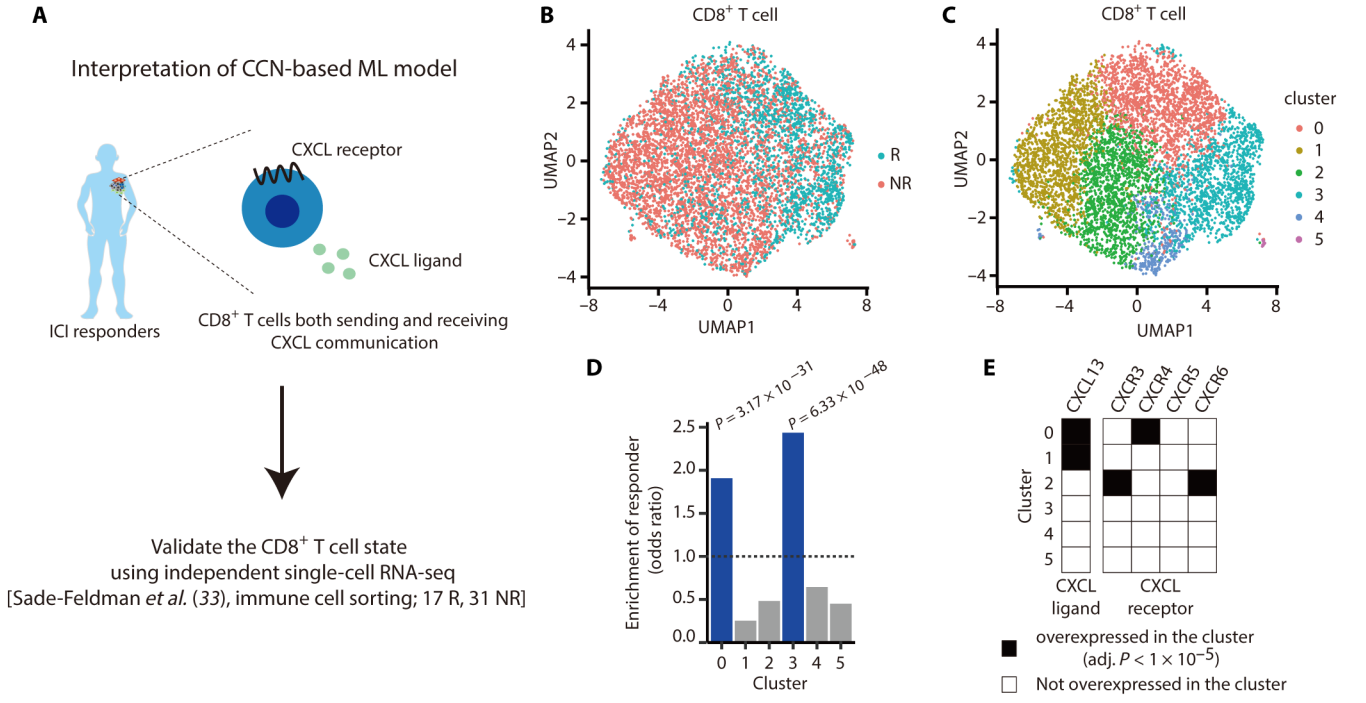

Fig. 4. Validation of CXCL-sending and CXCL-receiving CD8$^+$ T cells identified by CCN-based ML model in melanoma at the single-cell level. (**A**) Validation of the interpretation of the CCN-based ML model in melanoma at the single-cell level. (**B**) Uniform manifold approximation and projection (UMAP) representation of CD8$^+$T cells originating from melanoma patient samples for determining whether the cell was derived from responder (R) or nonresponder (NR). (**C**) UMAP representation showing subclusters of CD8$^+$T cells. (**D**) Enrichment of cells in CD8$^+$T cell subclusters to R-derived cells. *P* values were measured using the two-sided Fisher's exact test. (**E**) Test for overexpression of CXCL ligands and receptors in CD8$^+$T cell subclusters. The black rectangle indicated significant overexpression of the gene. Statistical significance was calculated using the two-sided Wilcoxon rank sum test adjusted by the Bonferroni method.

associated with patient response to ICIs using single-cell RNA sequencing (scRNA-seq) data of immune cells (CD45$^+$) derived from melanoma tumor samples of 17 R and 31 NR (*33*) as an independent ICI-treated cohort (Fig. 4A). CD8$^+$ T cells were extracted from the scRNA-seq data and divided into subclusters (Fig. 4, B and C). The subcluster "0," where R-derived cells were significantly enriched, overexpressed both the CXCL ligand (*CXCL13*) and the CXCL receptor (*CXCR4*) simultaneously (Fig. 4, D and E).

CCN-based ML model identifies chemotaxis-sending and chemotaxis-receiving immune-related cells as key factors for patient response to ICIs in NSCLC and BC

The CCN-based ML model identified CCL-sending and CCL-receiving immune cells as the key players for patient response to ICIs in NSCLC. The CCL pathway was identified as the key communication pathway in NSCLC because it exhibited the highest PIS (Fig. 5A and fig. S7). Moreover, the relationship between the CCL pathway and patient response to ICIs was validated using an independent cohort, (*34*). In the independent cohort, CCL communication probabilities could predict patient response to ICIs, and R had higher CCL probabilities than NR (Fig. 5, B and C). Furthermore, immune cells were identified as both key source and target cells because they exhibited the highest SIS and TIS simultaneously (Fig. 5, D and E).

The CCN-based ML model identified CXCL-sending macrophages and CXCL-receiving endothelial cells as the key players for patient response to ICIs in BC. The CXCL pathway was identified as the key communication pathway owing to the highest PIS (Fig. 5F and fig. S8). Furthermore, the association between the CXCL pathway and immunological activity of patients was validated. The more active the immune phenotype of BC patients was, the higher the CXCL communication occurred (Fig. 5G). To validate the association between CXCL and patient response to ICIs, the immune phenotype of each patient, assessed by the number of CD8$^+$ T cells that infiltrated the TIME using immunohistochemistry (IHC), was used. Macrophages were identified as the key source cells, as they exhibited the highest SIS (Fig. 5H), and endothelial cells were identified as the key target cells because they exhibited the highest TIS (Fig. 5I).

The CCN-based ML model identified major histocompatibility complex I (MHC-I)–sending and MHC-I–receiving immune cells as the key players behind patient response to ICIs in GC. The MHC-I communication pathway had the highest PIS in GC (figs. S9 and 10A), and immune cells exhibited both the highest SIS and TIS in the MHC-I pathway (fig. S10, B and C). MHC-I is involved in the activation of cytotoxic cells, such as CD8$^+$ T cells or natural killer (NK) cells, and their activities are important for ICI response (*1*, *35*). These results suggest that the prioritization of MHC-I–sending and MHC-I–receiving immune cells for patient response to ICIs is valid.

CCN-based ML model identifies MK-sending CAFs and MK-receiving B cells as key players behind resistance to ICI

Understanding the biology underlying resistance to ICIs can help establish a therapeutic strategy for patients with cancer (*22*, *23*). We found that the growth factor–mediated communication of structural

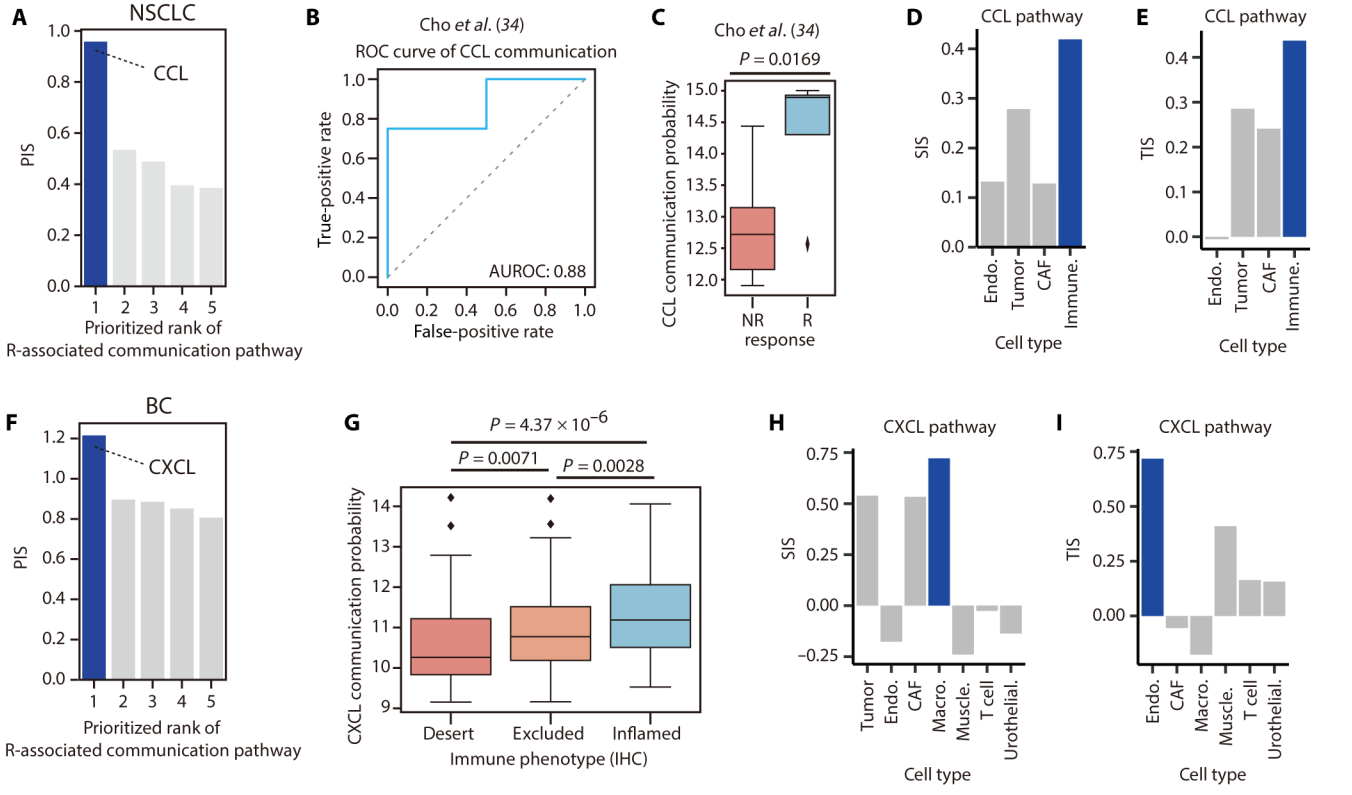

Fig. 5. CCN-based ML model identifies chemotaxis communication–sending and chemotaxis communication-receiving immune-related cells as the key for response to ICIs in NSCLC and BC. (**A**) CCL communication was prioritized as the key communication pathway in NSCLC. (**B** and **C**) Validation of the association of CCL communication with (B) predictability of response to ICIs and with (C) ICI responders/nonresponders in an independent NSCLC cohort (*34*). (**D** and **E**) Immune cells were prioritized as both the key source cells and the key target cells of the CCL communication pathway for response to ICIs by (D) SIS and (E) TIS, respectively. (**F**) Prioritization of CXCL communication pathway as the key communication pathway in BC. (**G**) CXCL communication pathway was related to immune phenotype measured by immunohistochemistry (IHC). (**H** and **I**) Identification of (H) the key source cell and (I) the key target cell in the CXCL communication pathway of BC. Statistical significance shown in (C) and (G) was calculated using the two-sided Mann-Whitney *U* rank test. Boxplots show median value, IQR as bounds of the box, and whiskers that extend from the box to upper/lower quartile ± IQR × 1.5. Abbreviation of cell types shown in (D), (E), (H), and (I): Immune cells, Immune.; muscle cells, Muscle.; and urothelial cells, Urothelial.

cells was the key biological process for resistance to ICIs across cancer types (Figs. 6 and 7).

The CCN-based ML model identified midkine (MK)–sending CAFs and MK-receiving B cells as the key players behind resistance to ICIs in melanoma. The model prioritized MK as the key communication pathway associated with resistance to ICIs because MK had the highest NR-associated PIS and exhibited a consistent association with NR (Fig. 6A and fig. S6). Furthermore, for the MK pathway, CAFs and B cells were the key source cells and key target cells for resistance to ICIs, respectively. CAFs and B cells exhibited the best average SIS and TIS, respectively, for resistance to ICIs (Fig. 6, B and C).

We validated that MK-sending CAFs and MK-receiving B cells were associated with resistance to ICIs in melanoma at the single-cell level, as identified by the CCN-based ML model (Fig. 6D). To confirm the relevance between MK-sending CAFs and ICI resistance, we tested whether NR-derived CAFs overexpressed the MK ligand using scRNA-seq data of 15 patients with melanoma (eight ICI NR and seven ICI treatment-naïve (TN) patients]. We elucidated that *MDK* expression levels, the only ligand of MK, of NR-derived CAFs were significantly higher than those of TN-derived CAFs (Fig. 6E and fig. S11, A and B). As the TN patients included both potential R and NR patients, *MDK* expression levels between NR-derived cells and TN-derived cells were compared, as described previously (*36*, *37*). Furthermore, to validate whether MK-receiving B cells were associated with resistance to ICIs, we tested whether NR-derived B cells overexpressed MK receptors. To this end, scRNA-seq data of immune cells obtained from 48 melanoma tumor samples from 31 NR and 17 R were analyzed. The expression levels of MK receptor genes in NR-derived B cells and R-derived B cells were compared. The NR-derived B cells significantly overexpressed *SDC1*, and *ITGA6*, MK receptor genes compared with that by the R-derived B cells (Fig. 6F and fig. S11, C to E).

The CCN-based ML model identified leukemia inhibitory factor receptor (LIFR)–sending CAFs and LIFR-receiving macrophages as the key players behind resistance to ICIs in BC. LIFR had the best PIS and exhibited the best association with resistance to ICIs in the BC cohort (fig. S8 and fig. S12A). The SIS of CAFs and the TIS of macrophages exhibited the strongest association with resistance to ICIs (fig. S12, B and C). LIFR acts as a growth factor and is relevant to macrophage-mediated resistance to ICIs (*38*, *39*). These suggested that the prioritization of LIFR-sending CAFs and LIFR-receiving macrophages by the CCN-based ML model is valid.

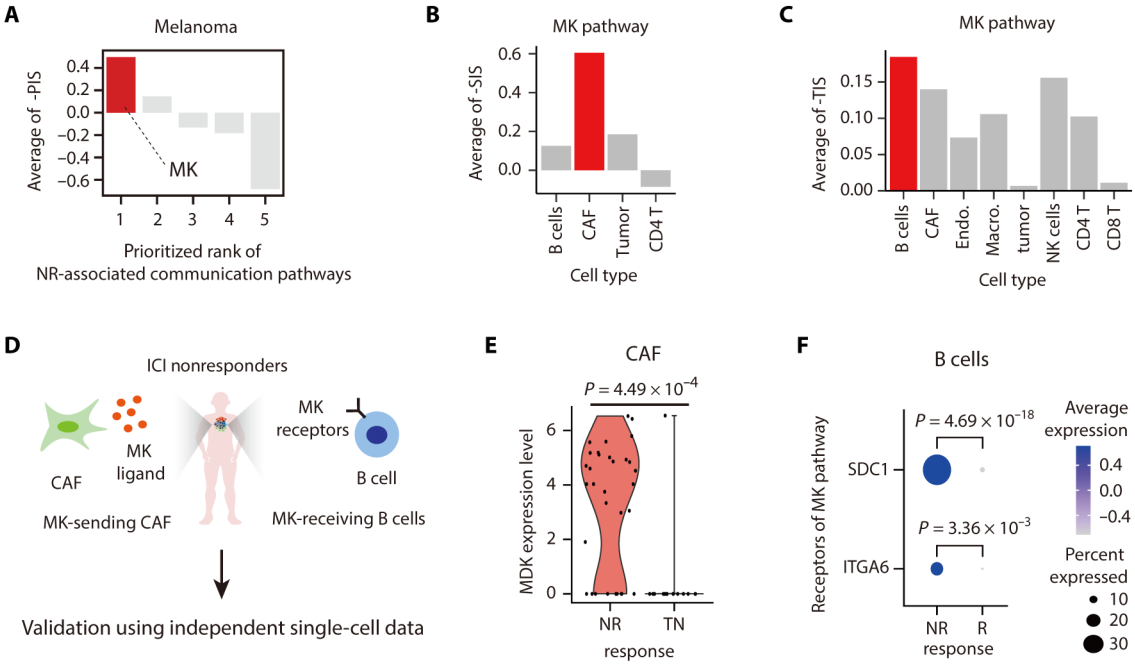

Fig. 6. Association of MK growth factor communication-sending CAFs and MK-receiving B cells with resistance to ICIs based on the interpretation of the CCN-based ML model in melanoma. (**A**) MK was prioritized as the key communication pathway based on its average PIS and consistent association with NR across four melanoma cohorts. (**B** and **C**) Prioritization of (B) CAFs as the key source cells and (C) B cells as the key target cells of the MK communication pathway for resistance to ICIs based on average of SIS and average of TIS across melanoma cohorts. (**D**) CCN-based ML model identified MK-sending CAFs and MK-receiving B cells as the key players for resistance to ICIs in melanoma, using single-cell transcriptome data. (**E**) Violin plots comparing expression levels of *MDK* between NR-derived CAFs and treatment-naïve (TN)–derived CAFs. Statistical significance was calculated using the Wilcoxon rank sum test. (**F**) Dot plots comparing expression levels of *SDC1* and *ITGA6* between NR-derived B cells and R-derived B cells. Dots were colored by average expression levels of indicated genes, and dot sizes were proportional to the percentage of cells expressing the indicated genes. Statistical significance was calculated using the Wilcoxon rank sum test adjusted by the Bonferroni method.

CCN-based ML model identifies growth factor–sending and growth factor–receiving tumors to be key factors for resistance to ICIs in NSCLC and GC

The CCN-based ML model identified growth factor–sending and growth factor–receiving tumors as the key players behind resistance to ICIs in the NSCLC and GC cohorts. The CCN-based ML model of NSCLC identified the fibroblast growth factor (FGF) pathway as the key communication pathway, as the PIS of FGF pathway exhibited the strongest association with NR (Fig. 7A and fig. S7). Moreover, the association between the FGF pathway and resistance to ICIs was validated using an independent cohort [cohort reported by Cho *et al.* (*34*)]. In the independent cohort, FGF communication probabilities predicted resistance to ICIs in patients with NSCLC, and NR tended to have higher FGF probabilities than R (Fig. 7, B and C). Furthermore, the CCN-based ML model of GC prioritized platelet-derived growth factor (PDGF) as the key communication pathway for resistance to ICIs. The PIS of PDGF exhibited the best association with NR (Fig. 7D and fig. S9). The association between the PDGF pathway and inactive immunological properties of patients in the GC cohort was validated by comparing the PDGF communication probabilities of patients with the "desert" TIME subtype to those of the patients with the "inflamed" TIME subtype. TIME immunological subtypes of the patients reported by (*40*) were used. The PDGF communication probabilities of the patients with the desert TIME subtype were higher than those of the patients with the inflamed TIME subtype (Fig. 7E). This is consistent with the previous result that the desert TIME subtype exhibited more inactive immune characteristics than the inflamed subtype.

The CCN-based ML model of NSCLC and GC identified tumors as both key source cells and key target cells. The SIS and TIS of tumors exhibited the best association with NR in NSCLC and GC (Fig. 7, F to I).

Furthermore, we undertook a comparative analysis between the key communication pathways delineated by CCN-based ML models and those derived from without CCN-based ML models to investigate shared elements. Key communication pathways of CCN-based ML models were differentially identified compared to those of without CCN-based ML models (i.e., without CCN in Fig. 2, A to I). In without CCN-based ML models, JAM and MHC-related pathways were the key pathways for response to ICIs, while NPFF, COLLAGEN, and PARs were the key pathways for resistance to ICIs (fig. S13). To this end, PIS for without CCN-based ML model was calculated to find key communication pathways of the models (Material and Methods). Notably, because of the absence of cellular features within the without CCN-based ML models, it failed to identify key source and target cells, suggesting that the superior interpretability of CCN-based ML models compared to those of without CCN-based ML models, not just superior predictive performances (Figs. 1B and 2, A to I).

Key communication pathways for resistance to ICIs are potential drug targets for ICI-based combinatorial therapies

ICI-based combinatorial therapies have been investigated to extend the clinical benefits of ICIs (*2*, *41*). Because the CCN-based ML model prioritized the communication pathways associated with resistance to ICIs in different types of cancer (Figs. 6 and 7), we

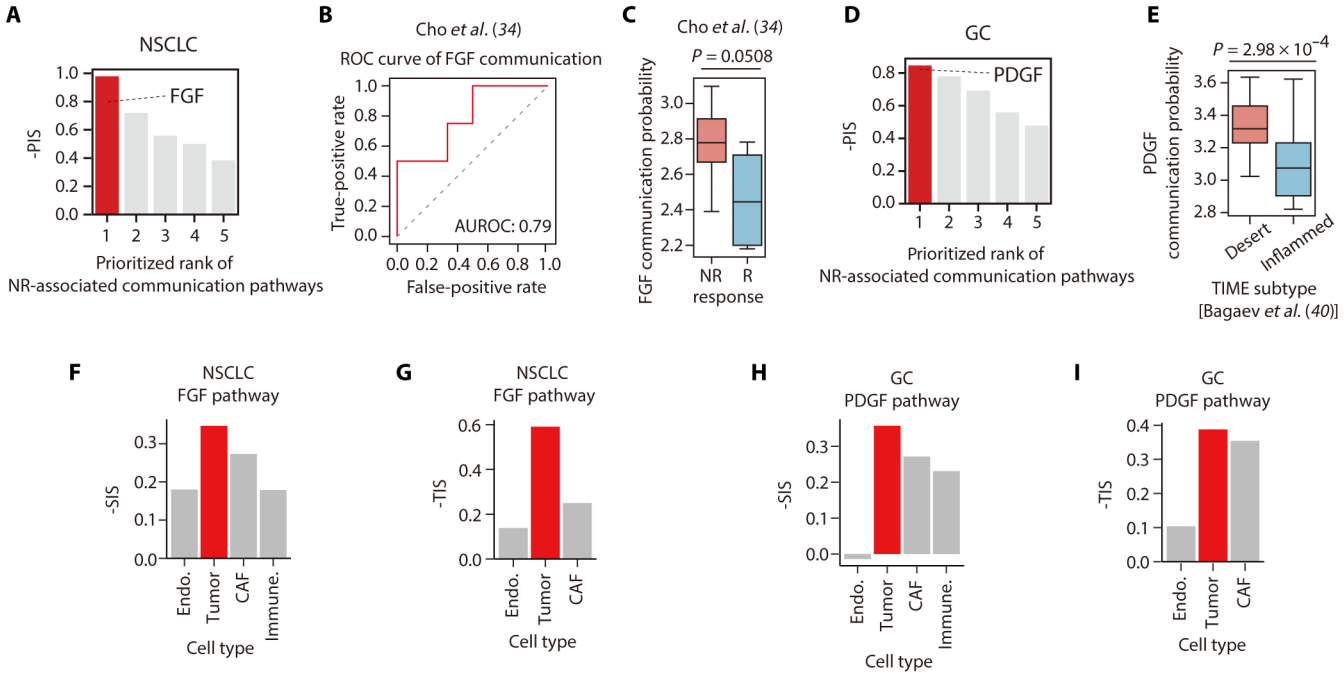

Fig. 7. CCN-based ML model identifies tumors sending and receiving growth factor–mediated communications as the key players for resistance to ICIs in NSCLC and GC. (**A**) Fibroblast growth factor was prioritized as the key communication pathway for resistance to ICIs in NSCLC. (**B** and **C**) Association of FGF with (B) predictability of resistance and (C) ICI efficacy in an independent NSCLC cohort (*34*). (**D**) Prioritization of the PDGF pathway as the key communication pathway for resistance to ICIs in GC. (**E**) Patients with the desert tumor immune microenvironment (TIME) subtype (immunosuppressive TIME subtype) showed higher PDGF communication probability than those with the inflamed subtype (immune-active TIME subtype). (**F** to **I**) Identification of key source cell and a key target cell in the FGF pathway of NSCLC and the PDGF pathway of GC. Tumors were prioritized as both the key source cell and the key target cell in [(F) and (G)] the FGF pathway of NSCLC and [(H) and (I)] the PDGF pathway of GC, respectively. Statistical significance shown in (C) and (E) was calculated using the two-sided Mann-Whitney *U* rank test. Boxplots show median value, IQR as bounds of the box, and whiskers that extend from the box to upper/lower quartile ± IQR × 1.5.

investigated whether these pathways could be the drug targets of ICI-based combinatorial therapies (Fig. 8A). We tested whether the genes involved in the MK, FGF, and PDGF communication pathways were enriched in the target genes of candidate drugs for ICI-based combinatorial therapies (Materials and Methods). We elucidated that the genes involved in the MK, FGF, and PDGF communication pathways were significantly enriched in the target genes of the candidate drug targets for ICI-based combinatorial therapies, suggesting that these pathways were potential targets for ICI-based combinatorial therapy (Fig. 8, B to D).

DISCUSSION

In this study, a CCN-based ML model was trained using cell-to-cell regulatory relationships to predict ICI efficacy in patients. The model exhibited better predictive performance for ICI efficacy than the gene-based ML model (Fig. 2). The links of the CCN constructed from the bulk transcriptome data of a patient with tumor represent cell-to-cell regulatory relationships occurring in the TIME of a patient (Fig. 1A and fig. S1). The efficacy of ICI in a patient is dependent on the immunological characteristics of its TIME (*42*). Cell-to-cell regulatory relationships are fundamental in shaping the immunological characteristics of the TIME (*42*, *43*). ICI therapy interferes with communications mediated by PD-1, PD-L1, and CTLA4 (*3*).

Single-cell (like) transcriptomes display cell-type gene expression profiles (Fig. 1A and fig. S1). We used single-cell–like transcriptomes deconvoluted from a patient's bulk tumor to build CCN. Understanding the underlying mode of action responsible for ICI efficacy is critical for expanding its clinical benefits. Single-cell (like) transcriptomes reveal the mode of action, as the same gene expressed by different cell types is used for different purposes. For example, PD-L1 expressed by APCs is used for inhibiting the excessive activation of T cells, whereas the same gene expressed by tumors is used for immune evasion (*44*, *45*). Previous studies investigating cell type–specific gene expression profiles of tumors revealed the mode of action for ICI efficacy. (*46*) identified the cellular ecosystems required for ICI efficacy using single-cell–like transcriptomic data. This suggests that coordination among T cells, B cells, and APCs is essential for patient response to ICIs (*46*). Zhang *et al.* (*37*) predicted patients' ICI efficacy based on cancer stemness signature genes identified using single-cell transcriptomic analysis. This study suggested that the stemness of cancer cells is important in determining ICI efficacy (*37*).

A subtype of $CD8^+$ T cells expressing both *CXCL13* and *CXCR4* was associated with patient response to ICIs in melanoma (Fig. 4). CCL-sending and CCL-receiving immune cells were prioritized as key players behind patient response to ICIs in NSCLC (Fig. 5, A to E). These results suggest that successive attraction among immune cells mediated by chemotaxis is a notable mode of action for patient response to ICIs. CXCL13, also called B cell attracting chemokine-1, recruits B cells to build a TLS in the TIME, which plays a major role in response to ICIs (*47*, *48*). CXCR4 guides the infiltration of $CD8^+$ T cells into solid tumors (*49*). CCL mediates response to ICIs by

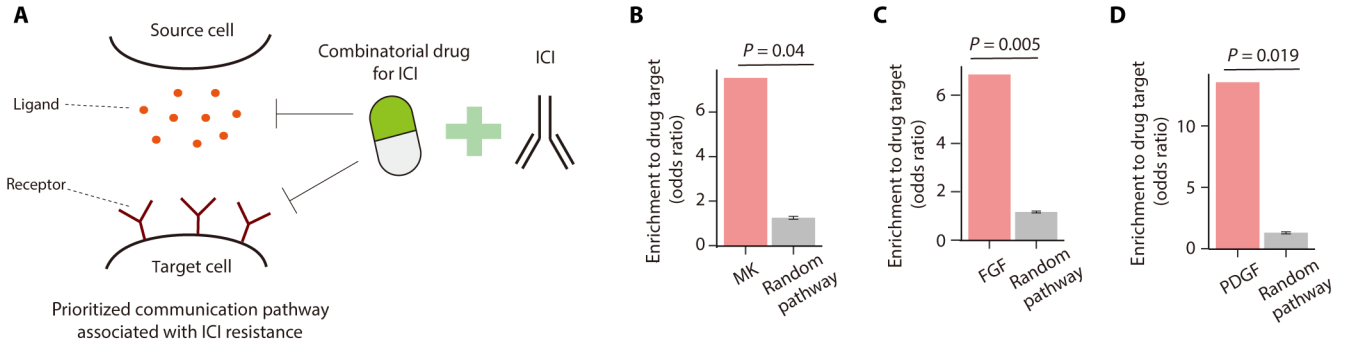

Fig. 8. Prioritized communication pathways associated with resistance to ICIs are potential drug targets for ICI-based combinatorial therapy. (**A**) A schematic concept of the prioritized communication pathways associated with resistance to ICIs as potential drug targets for ICI-based combinatorial therapy. (**B** to **D**) Enrichment of genes involved in (B) MK, (C) FGF, and (D) PDGF communication pathways to target genes of candidate drugs for ICI-based combinatorial therapy. Statistical significance was calculated using empirical *P* values by randomly permuting the genes involved in the communication for 1000 times.

recruiting dendritic cells (DCs) in the TIME to induce T cell expansion in NSCLC (*50*). Recently, the chemokine system of CAR-T was engineered to facilitate antitumor immunity in patients by provoking its homing into solid tumors (*51*).

CXCL-sending macrophages and CXCL-receiving endothelial cells were identified as the key players in patient response to ICIs in BC (Fig. 5, F to I). This suggests that vasculature normalization in the TIME is an important mode of action responsible for patient response to ICIs. Endothelial cells regulate immune cell infiltration into the vasculature (*52*). Notably, CXCL-receiving endothelial cells play a crucial role in vasculature normalization, which improves the patient response to ICIs (*53*). CXCL-sending macrophages induce response to ICIs by recruiting $CD8^+$ T cells (*54*).

MK-sending CAFs and MK-receiving B cells were prioritized as key players in resistance to ICIs in melanoma (Fig. 6). This suggests that the immunosuppressive TIME created by structural cell–derived growth factors raises resistance to ICIs. This is supported by the experimental results of a previous study that melanoma cells overexpressing the MK ligand (*MDK* gene) give rise to an immunosuppressive TIME and resistance to ICIs (*55*); however, administration of ICI with an MK inhibitor restored response to ICIs (*55*). These results are consistent with our finding that the MK communication pathway is a potential drug target for ICI-based combinatorial therapies (Fig. 8A).

Growth factor–sending and growth factor–receiving tumors were identified as the key player behind resistance to ICIs in NSCLC and GC (Fig. 7). This suggests that aggressive tumor growth, stimulated by growth factors, leads to resistance to ICIs. Overexpression of FGF in the lungs induces rapid tumorigenesis and resistance to ICIs in NSCLC (*56*, *57*). However, treatment with an FGFR inhibitor and ICI recovered the response to ICIs in an NSCLC tumor-intrinsic manner (*57*). Furthermore, GC cells express PDGF ligands and receptors to promote their growth (*58*, *59*). These results are in line with our results that FGF and PDGF pathways are a potential drug target for ICI-based combinatorial therapies (Fig. 8, B and C).

Recently, single-cell transcriptome data of patients with tumors have rapidly accumulated (*60*). This study provides a way to expand the use of single-cell transcriptome data for cancers. In our study, the key communication pathways correlated with the immune phenotype of the patient TIME (Figs. 5G and 7E), but we investigated on four to eight cell types depending on the cancer type (Fig. 1A and fig. S1), which limited the investigation of other important cell types associated with TIME, including T_{reg} and DCs. In the future, CCN can be applied to depict a detailed cell-to-cell regulation based on a cell atlas to improve ICI efficacy predictions (*61*, *62*).

MATERIALS AND METHODS

Collection and preprocessing of data of ICI-treated cancer patients

We collected data from nine independent cohorts for investigating bulk tumor transcriptomes of patients and from two independent cohorts for investigating single-cell transcriptomes of patients with melanoma. Bulk RNA sequencing (RNA-seq) data of tumors was obtained from the datasets reported by the following studies: (i) VanAllen *et al.* (*24*), (ii) Liu *et al.* (*25*), (iii) Gide *et al.* (*26*), (iv) Hugo *et al.* (*27*), (v) Jung *et al.* (*28*), (vi) Kim *et al.* (*30*), (vii) Mariathasan *et al.* (*29*), (viii) Prat *et al.* (*32*), and (ix) Cho *et al.* (*34*). scRNA-seq data for melanoma tumors were obtained from the datasets reported by the following studies: (i) Sade-Feldman *et al.* (*33*) and (ii) Jerby-Anon *et al.* (*36*).

For the Gide, Hugo, Jung, Kim, and Cho datasets, fastq files of the patient data were downloaded and aligned to the human reference genome GRCh38 using STAR (v 2.7.9a) (*63*). Read counts were calculated using the RSEM pipeline (v 1.3.3) (*64*). For the Mariathasan dataset, the read counts were downloaded. The gene expression levels were calculated by normalizing the counts as per the trimmed means of *M* value normalization using the edgeR R package (v 3.32.1) (*65*, *66*). For the VanAllen, Liu, and Prat datasets, we used the processed gene expression levels provided by (*67*) (VanAllen and Liu datasets) or Gene Expression Omnibus (GEO) (Prat dataset). The processed gene expression levels were downloaded using the GEOquery R package (v. 2.58.0). For the Sade-Feldman and Jerby-Arnon datasets, we used processed gene expression levels, cell-type annotation data, and clinical information obtained from the GEO repository and the supplementary tables of original papers (*33*, *36*).

For drug response labels, the patients with partial response and complete response were classified as R, and the patients with stable disease and progressive disease were classified as NR when RECIST was used to evaluate efficacy. For the VanAllen cohort, R and NR were classified according to the criteria reported by Lee *et al.* (*67*), and the labels provided by the original papers were used for the Sade-Feldman and Jerby-Arnon cohorts. Detailed description of the datasets used in this study is provided in data S1.

Deconvolution of bulk tumor transcriptome of patients with cancer into cell type–specific gene expression profiles

To extract cell type–specific gene expression profiles from the bulk tumor transcriptome of patient with cancer, we used CIBERSORTx "high-resolution mode" (CIBERSORTx-hires, v1.0), implemented through Docker. CIBERSORTx is a well-validated computation tool for deconvoluting bulk transcriptome into cell-type gene expression profiles (*17*), and cell-type gene expression profiles deconvoluted using CIBERSORTx have been used to identify distinct cell states within tumor microenvironments and tumor ecosystem subtypes (*46*). CIBERSORTx-hires requires the following two types of inputs: a mixture and a signature matrix. A mixture was gene expression levels of bulk tumor derived from patients. Its rows corresponded to gene symbols, and columns corresponded to samples. CIBERSORTx-hires deconvoluted the mixture into cell type–specific gene expression profiles by referring to the signature matrix. The rows of the signature matrix corresponded to the signature gene symbol of a cell type, and the columns corresponded to cell types.

We used a signature matrix derived from a tissue type compatible with the cancer type of the patient. For the deconvolution of bulk tumor transcriptome data of patients with melanoma, we used a signature matrix derived from melanoma samples; for the deconvolution of the transcriptomes of patients with NSCLC and patients with GC, we used the TR4 signature gene expression profile, according to a previous study (*46*). Signature matrices of melanoma and TR4 were previously developed and are publicly available (*17*, *46*). To deconvolute the bulk tumor transcriptome data of patients with BC, we created a signature matrix using scRNA-seq data of a patient with BC (*68*) using the CIBERSORTx framework with default settings (data S2).

To implement CIBERSORTx through Docker, we used the options of rmbatchBmode TRUE and QN FALSE, as previously described (*46*). It returned matrices with genes in rows and samples in the column across cell types. Consequently, the bulk tumor transcriptome data of patients with melanoma were deconvoluted into eight cell types (tumor, CAFs, endothelial cells, B cells, macrophages, NK cells, CD4 T cells, and CD8 T cells), the transcriptome of patients with NSCLC or GC into four cell types (tumor, CAFs, endothelial cells, and immune cells), and the transcriptome of patients with BC into seven cell types (tumor, CAFs, endothelial cells, macrophages, urothelial cells, muscle cells, and T cells) (Fig. 1A and fig. S1). The deconvoluted cell type–specific gene expression profiles were further processed to calculate the communication probabilities between two cells. Gene expression levels inferred as not available (NA) were set to 0, log-transformed after adding 1 to the expression values, and quantile-normalized using the normalize.quantiles of the preprocessCore R package (v 1.52.1).

Construction of CCNs

The CCN of a patient consisted of the cell type as a node and the communication strength between cells as a link. We adopted CellChat to measure the communication strength between two cells called the communication probability. CellChat quantitatively inferred communication probability using the gene expression levels of the ligands, receptors, and cofactors of each cell type (*18*). To calculate communication probability, CellChat exploits the Hill function, an equation that delineates the binding between ligands and receptors in biochemistry, and its own database containing data about relationships between ligands, receptors, and cofactors. Consequently, the communication probability represents the communication strength between a cell expressing the ligand gene (source cell; denoted as ligand A in Fig. 1A) and a cell expressing the receptor gene (target cell; denoted as receptor A in Fig. 1A).

To calculate communication probability using deconvoluted cell type–specific gene expression profiles, we modified some parts of the CellChat. Originally, CellChat uses the representative expression values of the overexpressed genes in each cell type using scRNA-seq data to obtain communication probabilities. We modified CellChat to calculate communication probabilities using all ligand-receptor pairs from the deconvoluted cell type–specific gene expression values. CIBERSORTx provided representative gene expression values of cell types, and we wanted to construct a comprehensive CCN of a patient, not just overexpressed ligand/receptors.

We integrated the communication probabilities of ligand-receptor pairs with similar biological functions into a single communication probability of a specific pathway. To take the biological functions into account, CellChat collected ligand-receptor pairs that have a similar biological function into a single communication pathway (denoted as pathways A, B, C, D, …, in Fig. 1A and fig. S1). We used "computeCommunProbPathway" function of CellChat R package (v 1.1.0) to do this, which summed up communication probabilities of ligand-receptor pairs involved in the same pathway according to their empirical *P* values. The *P* values were obtained by randomly permuting the cell-type labels to evaluate the calculated communication probabilities. Because the *P* value depended on the number of cell types, we used the function with default setting if the number of cell types was equal to or more than seven (i.e., melanoma and BC) or without a permutation threshold if the number of cell types was four (i.e., when the TR4 signature matrix was used). Therefore, CCN was constructed by measuring communication probabilities between the source and target cells across communication pathways from bulk tumor transcriptome data of patients with cancer (Fig. 1A and fig. S1). For randomized CCN, we randomly permuted the ligand-receptor-cofactor relationships and calculated the communication probabilities.

ML model for prediction of response of patients with cancer to ICI

We used the logistic regression model provided by Scikit-learn (v 0.24.2) in Python as an interpretable ML model. We adopted the "balanced" parameter for class_weight hyperparameters to avoid the effect of class imbalance and the "liblinear" parameter for solver hyperparameter because Scikit-learn suggested it to be suitable for small datasets, otherwise default setting was used. For the CCN-based ML model, communication probabilities were used as the independent variable for the model. For gene-based or cell-type proportion-based ML models, gene expression levels or cell-type proportions inferred by CIBERSORTx were used as independent variables, respectively. For the gene expression levels, the expression levels of ICI target genes (*PD1*, *PD-L1*, and *CTLA4*) and TIME-associated genes [gene sets associated with CAFs, CD8T cells, and T cell exhaustion (T exhaust.), TAM, and communication (comm.)] were used (*6*, *31*). Moreover, the predictive performance of the ML model trained using all ICI target genes (drug targets) and the expression of the all TIME-associated genes [TIME.] was compared to that of the CCN-based ML model. Specific features and the number of features used for the ML models were summarized in table S1 and data S3. The cellular proportions are known to be informative for

the prediction of patient response to ICIs (*17*, *69*), and the construction of CCN was based on cell type–specific gene expression profiles by deconvolution of the bulk tumor transcriptome (Fig. 1A and fig. S1). Patient responses to ICIs were the dependent variables for each model. For every independent variable, *z* score standardization was applied across patients to normalize the scale of features using the fit_transform function of the sklearn.preprocessing. StandardScaler python module.

To effectively train the ML model using communication probabilities, NetBio detection, which we developed in our previous study to select biological pathways proximal to drug targets in a protein-protein interaction (PPI) network, was applied as previously described with some modifications (*21*). For drug targets, we used the following ICI targets administered to patients in each cohort: CTLA-4 for the VanAllen cohort; PD-1 for the Liu, Hugo, and Kim cohorts; PD-1 and CTLA-4 for the Gide cohort; PD-L1 for the Mariathasan cohort; and PD1 and PD-L1 for the Jung cohort. The network propagation score was calculated using the PageRank algorithm with drug targets as 1 and the others as 0 in the PPI network (STRING v.11.0) (data S4 to S8). Communication pathways significantly enriched in the top 3000 genes with high network propagation scores were selected to train the ML model. Significance of enrichment was measured using a hypergeometric test, the *P* values were corrected using the Benjamini/Hochberg method, and adjusted *P* values lower than 0.05 were considered significant.

Leave-one-out cross-validation (LOOCV) was performed to evaluate the predictive performance of the ML model. In each cohort, training set comprised features from all patients except for one (i.e., leaving one out of the cohort), and test set consisted of the features from the one patient who was excluded from the training set. The AUROC curve and the area under the precision-recall curve were used as the metrics of predictive performance. Predictive performance was measured using the prediction outcomes of the test set. The number of patients used for training and testing the ML model from each cohort have been listed in data S9.

To analyze the effect of cancer-type specificity on predictive performances of ICI efficacy, we merged seven cohorts used for LOOCV in Fig. 2 into a single cohort. To this end, we carried out batch correction using ComBat of sva R package (v. 3.38.0) (*70*). The bulk tumor transcriptomes of merged cohort, which contain four different cancer types of samples, were deconvoluted into cell-type gene expression profiles by CIBERTSORTx using signature matrices of melanoma, BC, and TR4, respectively, to extract cell-type gene expression profiles irrelevant to the cancer type of a patient. Then, CCN was constructed using the cell-type gene expression profiles. The predictive performances of cancer-type nonspecific CCN-based ML models were evaluated using LOOCV, and AUROC was used as a metric.

Identification of key communication pathways, source cells, and target cells based on CCN-based ML model

To identify key communication pathways, source cells, and target cells from the CCN-based ML model, we calculated PIS, SIS, and TIS using feature importance. To calculate these scores, the feature importance of the communication probabilities obtained from the trained CCN-based ML model (coef_ attribute) was used. The feature weight was measured for each test set, and the average feature weight across the test sets was adopted as the feature importance.

The PIS was calculated by the summation of all feature importance in a communication pathway. A communication pathway was related to R (i.e., patient response to ICIs) at PIS > 0. In contrast, a pathway was related to NR (i.e., resistance to ICIs) at PIS < 0 (Fig. 3A). Therefore, the communication pathway with the highest PIS was designated as the key communication pathway for response to ICIs. The communication pathway with the lowest PIS was designated as the key pathway for resistance to ICIs. For melanoma, we used the average PIS across the four melanoma datasets used for LOOCV. In addition, we used sign consistency of PIS across the melanoma datasets (i.e., consistent positive or negative PIS across datasets) to identify key communication pathways because a consistent sign of PIS indicated a robust association with either response or resistance to ICIs.

SIS and TIS were calculated by the summation of the outward and inward feature importance of a cell in a communication pathway, respectively (Fig. 3, E and G). The cell that exhibited the highest SIS was designated as a key source cell for response to ICIs, whereas the cell with the lowest SIS was designated as a key source cell for resistance to ICIs. Similarly, the cell with the highest or lowest TIS was designated as the key target cell for response or resistance to ICIs, respectively.

To compare key communication pathways between CCN-based ML models and without CCN-based ML models (i.e. without CCN in Fig. 2, A to I), we introduced an additional PIS for without CCN-based ML models. PIS for without CCN-based ML models were calculated by the summating all feature importance of genes involved in one communication pathway. Without CCN-based ML models were trained by expression levels of genes that go into CCN-based ML models (Fig. 2A).

Validating the relevance of key communication pathway with ICI efficacy or immune phenotype of patients

To analyze whether key communication pathways were associated with ICI efficacy of the independent cohort or TIME phenotype, we calculated pathway-level communication, such as CXCL communication probability. Pathway-level communication was calculated by the summation of all communication probabilities between the source and target cells in the pathway.

For melanoma, (*32*) cohort with 25 patients (R: 9, NR: 16; data S9) was analyzed as an independent ICI-treated melanoma cohort. The CXCL communication probabilities of R were compared with those of NR. To investigate the effect of the CXCL communication pathway on patient survival, patients with CXCL communication probability higher than or equal to the median of the communication were grouped in the high CXCL communication probability group, whereas others were grouped in the low CXCL communication probability group. Survival analysis was performed using the survival (v3.2.10) and survminer R packages (v0.4.9).

For NSCLC, (*34*) cohort with 16 patients (R: 4, NR: 12, data S9) was adopted as an independent ICI-treated NSCLC cohort. To analyze the association of CCL and FGF communication pathways with response and resistance to ICIs, respectively, the CCL and FGF communication probabilities of R were compared to those of NR. Moreover, to test whether CCL and FGF communication pathways could predict R and NR, respectively, the AUROC was measured using their communication probabilities.

For BC, the immune phenotype labels of patients based on the number of $CD8^+$ T cells infiltrating the tumor as measured by IHC were used. The phenotypes were classified into immune desert, excluded, and inflamed according to the prevalence and infiltration pattern

of $CD8^+$ T cells. To analyze the relevance of the CXCL communication pathway to the immune phenotype, CXCL communication probabilities in patients were compared according to their immune phenotypes.

For GC, the TIME phenotype labels of patients annotated by (*40*) were used. (*40*) classified TIME into the following four subtypes: immune-enriched fibrotic (IE/F), immune-enriched nonfibrotic (IE), fibrotic (F), and desert (D). They considered IE/F and IE subtypes as immune-inflamed and F and D as immune deserts. To analyze the association of the PDGF communication pathway with TIME phenotypes, PDGF communication probabilities of patients with inflamed TIME phenotypes were compared to those of patients with desert TIME phenotypes.

Analysis of scRNA-seq data obtained from melanoma patients

To validate whether the key players identified from the melanoma CCN-based ML model were associated with response or resistance to ICIs, single-cell transcriptome datasets of ICI-treated patients with melanoma reported by Sade-Feldman *et al.* (*33*) and Jerby-Arnon *et al.* (*36*) were used. The processed expression values and metadata of individual cells were downloaded from the GEO repository and incorporated into the Seurat object (v 4.0.2). Principal components analysis was applied using the RunPCA function of the Seurat R package based on variable features identified by the FindVariableFeatures function followed by scaling. We followed the cell-type annotations provided in supplementary tables of the original papers.

To analyze the gene expression levels of $CD8^+$ T and B cells, the single-cell transcriptomic dataset reported by Sade-Feldman *et al.* (*33*), which revealed gene expression profiles of immune cells derived from ICI-treated melanoma patient tumor samples, was used. To analyze the $CD8^+$ T cell subcluster, we followed the clustering tutorial of the Seurat package (https://satijalab.org/seurat/articles/pbmc3k_tutorial.html). Briefly, $CD8^+$ T cells were extracted, subclusters of $CD8^+$ T cells were identified using the FindNeighbors and FindClusters functions, and the genes overexpressed in each cluster were identified using the FindAllMarkers function. For the analysis of B cells, they were extracted, and gene expression levels of MK receptors were compared between NR-derived B cells and R-derived B cells using the FindMarkers function. The cells annotated as B cells and plasma cells were considered as B cells.

To analyze the gene expression levels of CAFs, we used the dataset reported by (*36*). The cells annotated as CAFs were extracted, and gene expression levels of the MK ligand (MDK) were compared between NR-derived CAFs and TN-derived CAFs using the FindMarkers function. This dataset included data reported by the (*71*) and data from "New" cohorts. We used the single-cell transcriptome data of New cohorts to split discovery and validation datasets because the signature matrix used for the deconvolution of the bulk tumor transcriptome data of patients with melanoma was constructed using single-cell transcriptome data reported in (*17*, *71*).

Enrichment analysis of key communication pathways for resistance to ICIs as potential drug targets for ICI-based combinatorial therapy

To investigate whether the key communication pathways for resistance to ICIs could act potential therapeutic targets for ICI-based combinatorial therapy, we tested whether the genes involved in the key communication pathway were enriched in the potential drug targets of for ICI-based combinatorial therapy. We manually curated a list of 19 candidate compounds that are being tested in combination with ICI in at least more than phase 2 (*72*–*74*). The drug targets of these compounds were collected using the following two sources of drug-target interactions: (i) DrugBank (v 5.1.9) (*75*) and (ii) STITCH (v 5.0) (*76*). For the DrugBank database, we considered only the pharmacological targets, excluding enzymes, carriers, and transporters. For the STITCH database, we considered the drug-target interactions with a combined interaction score of $\geq$700. We used the union of genes from the two sources as potential drug targets of ICI-based combinatorial therapy (data S10). The genes involved in the key communication pathways for resistance to ICIs were collected from CellChatDB.human of the CellChat R package (v1.1.0). The statistical significance of the enrichment of the communication genes in the candidate drug targets for ICI-based combinatorial therapy was measured by empirical *P* values using the same number of randomly selected genes with genes of the communication pathway 1000 times.

Statistical analyses

To evaluate statistical significance of predictive performances shown in Fig. 2 (I and Q), and fig. S3I, the two-sided Wilcoxon signed-rank test was used. To calculate statistical significances of pathway-level communication probabilities shown in Figs. 3C, 5 (C and G), and 7 (C and E) and predictive performance shown in fig. S4, the two-sided Mann-Whitney *U* rank test was used. For survival analysis shown in Fig. 3D, the two-sided log-rank test was used. For testing the significance of enrichment of R-derived cells for each $CD8^+$ T cell subcluster shown in Fig. 4D, the two-sided Fisher's exact test was used. For testing the significance of drug target enrichment shown in Fig. 8 (B to D), empirical *P* value was used by random permutation for 1000 times. For testing differential expression levels of genes in the single cell shown in Figs. 4E and 6 (E and F), Wilcoxon rank sum test was used, and Bonferroni correction was used to adjust the *P* value if the statistical test was multiple tests.

Supplementary Materials

This PDF file includes:

Fig. S1 to S13
Table S1
Legends for data S1 to S10

Other Supplementary Material for this manuscript includes the following:

Data S1 to S10

REFERENCES AND NOTES

1. A. D. Waldman, J. M. Fritz, M. J. Lenardo, A guide to cancer immunotherapy: From T cell basic science to clinical practice. *Nat. Rev. Immunol.* **20**, 651–668 (2020).
2. C. Schmidt, The benefits of immunotherapy combinations. *Nature* **552**, S67–S69 (2017).
3. S. C. Wei, C. R. Duffy, J. P. Allison, Fundamental mechanisms of immune checkpoint blockade therapy. *Cancer Discov.* **8**, 1069–1086 (2018).
4. M. L. Dustin, A. C. Chan, Signaling Takes Shape in the Immune System. *Cell* **103**, 283–294 (2000).
5. H. Raskov, A. Orhan, J. P. Christensen, I. Gögenur, Cytotoxic CD8+ T cells in cancer and cancer immunotherapy. *Br. J. Cancer* **124**, 359–367 (2021).
6. P. Jiang, S. Gu, D. Pan, J. Fu, A. Sahu, X. Hu, Z. Li, N. Traugh, X. Bu, B. Li, J. Liu, G. J. Freeman, M. A. Brown, K. W. Wucherpfennig, X. S. Liu, Signatures of T cell dysfunction and exclusion predict cancer immunotherapy response. *Nat. Med.* **24**, 1550–1558 (2018).
7. M. Philip, A. Schietinger, CD8+ T cell differentiation and dysfunction in cancer. *Nat. Rev. Immunol.* **22**, 209–223 (2022).
8. J. A. Joyce, D. T. Fearon, T cell exclusion, immune privilege, and the tumor microenvironment. *Science* **348**, 74–80 (2015).
9. R. Bai, Z. Lv, D. Xu, J. Cui, Predictive biomarkers for cancer immunotherapy with immune checkpoint inhibitors. *Biomark Res.* **8**, 34 (2020).

10. S. P. Patel, R. Kurzrock, PD-L1 Expression as a Predictive Biomarker in Cancer Immunotherapy. *Mol. Cancer Ther.* **14**, 847–856 (2015).
11. D. P. Carbone, M. Reck, L. Paz-Ares, B. Creelan, L. Horn, M. Steins, E. Felip, M. M. van den Heuvel, T.-E. Ciuleanu, F. Badin, N. Ready, T. J. N. Hiltermann, S. Nair, R. Juergens, S. Peters, E. Minenza, J. M. Wrangle, D. Rodriguez-Abreu, H. Borghaei, G. R. Blumenschein, L. C. Villaruz, L. Havel, J. Krejci, J. Corral Jaime, H. Chang, W. J. Geese, P. Bhagavatheeswaran, A. C. Chen, M. A. Socinski, CheckMate 026 Investigators, First-line nivolumab in stage IV or recurrent non–small-cell lung cancer. *N. Engl. J. Med.* **376**, 2415–2426 (2017).
12. K. Wu, M. Yi, S. Qin, Q. Chu, X. Zheng, K. Wu, The efficacy and safety of combination of PD-1 and CTLA-4 inhibitors: A meta-analysis. *Exp. Hematol. Oncol.* **8**, 26 (2019).
13. A. Taylor, J. Verhagen, K. Blaser, M. Akdis, C. A. Akdis, Mechanisms of immune suppression by interleukin-10 and transforming growth factor-beta: The role of T regulatory cells. *Immunology* **117**, 433–442 (2006).
14. J. S. Khalili, S. Liu, T. G. Rodríguez-Cruz, M. Whittington, S. Wardell, C. Liu, M. Zhang, Z. A. Cooper, D. T. Frederick, Y. Li, M. Zhang, R. W. Joseph, C. Bernatchez, S. Ekmekcioglu, E. Grimm, L. G. Radvanyi, R. E. Davis, M. A. Davies, J. A. Wargo, P. Hwu, G. Lizée, Oncogenic BRAF(V600E) promotes stromal cell-mediated immunosuppression via induction of interleukin-1 in melanoma. *Clin. Cancer Res.* **18**, 5329–5340 (2012).
15. N. Zhang, M. J. Bevan, CD8+ T cells: Foot soldiers of the immune system. *Immunity* **35**, 161–168 (2011).
16. G. S. Kinker, G. A. F. Vitiello, W. A. S. Ferreira, A. S. Chaves, V. C. C. de Lima, T. da Silva Medina, B Cell Orchestration of Anti-tumor Immune Responses: A Matter of cell localization and communication. *Front. Cell Dev. Biol.* **9**, 678127 (2021).
17. A. M. Newman, C. B. Steen, C. L. Liu, A. J. Gentles, A. A. Chaudhuri, F. Scherer, M. S. Khodadoust, M. S. Esfahani, B. A. Luca, D. Steiner, M. Diehn, A. A. Alizadeh, Determining cell type abundance and expression from bulk tissues with digital cytometry. *Nat. Biotechnol.* **37**, 773–782 (2019).
18. S. Jin, C. F. Guerrero-Juarez, L. Zhang, I. Chang, R. Ramos, C.-H. Kuan, P. Myung, M. V. Plikus, Q. Nie, Inference and analysis of cell-cell communication using CellChat. *Nat. Commun.* **12**, 1088 (2021).
19. C. Fan, L. Zeng, Y. Sun, Y.-Y. Liu, Finding key players in complex networks through deep reinforcement learning. *Nat. Mach. Intell.* **2**, 317–324 (2020).
20. J. Kong, H. Lee, D. Kim, S. K. Han, D. Ha, K. Shin, S. Kim, Network-based machine learning in colorectal and bladder organoid models predicts anti-cancer drug efficacy in patients. *Nat. Commun.* **11**, 5485 (2020).
21. J. Kong, D. Ha, J. Lee, I. Kim, M. Park, S.-H. Im, K. Shin, S. Kim, Network-based machine learning approach to predict immunotherapy response in cancer patients. *Nat. Commun.* **13**, 3703 (2022).
22. M. Vanneman, G. Dranoff, Combining immunotherapy and targeted therapies in cancer treatment. *Nat. Rev. Cancer* **12**, 237–251 (2012).
23. S. Zhu, T. Zhang, L. Zheng, H. Liu, W. Song, D. Liu, Z. Li, C. Pan, Combination strategies to maximize the benefits of cancer immunotherapy. *J. Hematol. Oncol.* **14**, 156 (2021).
24. E. M. van Allen, D. Miao, B. Schilling, S. A. Shukla, C. Blank, L. Zimmer, A. Sucker, U. Hillen, M. H. Geukes Foppen, S. M. Goldinger, J. Utikal, J. C. Hassel, B. Weide, K. C. Kaehler, C. Loquai, P. Mohr, R. Gutzmer, R. Dummer, S. Gabriel, C. J. Wu, D. Schadendorf, L. A. Garraway, Genomic correlates of response to CTLA-4 blockade in metastatic melanoma. *Science* **350**, 207–211 (2015).
25. D. Liu, B. Schilling, D. Liu, A. Sucker, E. Livingstone, L. Jerby-Arnon, L. Zimmer, R. Gutzmer, I. Satzger, C. Loquai, S. Grabbe, N. Vokes, C. A. Margolis, J. Conway, M. X. He, H. Elmarakeby, F. Dietlein, D. Miao, A. Tracy, H. Gogas, S. M. Goldinger, J. Utikal, C. U. Blank, R. Rauschenberg, D. von Bubnoff, A. Krackhardt, B. Weide, S. Haferkamp, F. Kiecker, B. Izar, L. Garraway, A. Regev, K. Flaherty, A. Paschen, E. M. van Allen, D. Schadendorf, Integrative molecular and clinical modeling of clinical outcomes to PD1 blockade in patients with metastatic melanoma. *Nat. Med.* **25**, 1916–1927 (2019).
26. T. N. Gide, C. Quek, A. M. Menzies, A. T. Tasker, P. Shang, J. Holst, J. Madore, S. Y. Lim, R. Velickovic, M. Wongchenko, Y. Yan, S. Lo, M. S. Carlino, A. Guminski, R. P. M. Saw, A. Pang, H. M. McGuire, U. Palendira, J. F. Thompson, H. Rizos, I. P. da Silva, M. Batten, R. A. Scolyer, G. V. Long, J. S. Wilmott, Distinct immune cell populations define response to anti-PD-1 Monotherapy and Anti-PD-1/Anti-CTLA-4 combined therapy. *Cancer Cell* **35**, 238–255.e6 (2019).
27. W. Hugo, J. M. Zaretsky, L. Sun, C. Song, B. H. Moreno, S. Hu-Lieskovan, B. Berent-Maoz, J. Pang, B. Chmielowski, G. Cherry, E. Seja, S. Lomeli, X. Kong, M. C. Kelley, J. A. Sosman, D. B. Johnson, A. Ribas, R. S. Lo, Genomic and transcriptomic features of response to anti-PD-1 therapy in metastatic melanoma. *Cell* **165**, 35–44 (2016).
28. H. Jung, H. S. Kim, J. Y. Kim, J.-M. Sun, J. S. Ahn, M.-J. Ahn, K. Park, M. Esteller, S.-H. Lee, J. K. Choi, DNA methylation loss promotes immune evasion of tumours with high mutation and copy number load. *Nat. Commun.* **10**, 4278 (2019).
29. S. Mariathasan, S. J. Turley, D. Nickles, A. Castiglioni, K. Yuen, Y. Wang, E. E. Kadel III, H. Koeppen, J. L. Astarita, R. Cubas, S. Jhunjhunwala, R. Banchereau, Y. Yang, Y. Guan, C. Chalouni, J. Ziai, Y. Şenbabaoğlu, S. Santoro, D. Sheinson, J. Hung, J. M. Giltnane, A. A. Pierce, K. Mesh, S. Lianoglou, J. Riegler, R. A. D. Carano, P. Eriksson, M. Höglund, L. Somarriba, D. L. Halligan, M. S. van der Heijden, Y. Loriot, J. E. Rosenberg, L. Fong, I. Mellman, D. S. Chen, M. Green, C. Derleth, G. D. Fine, P. S. Hegde, R. Bourgon, T. Powles, TGFβ attenuates tumour response to PD-L1 blockade by contributing to exclusion of T cells. *Nature* **554**, 544–548 (2018).
30. S. T. Kim, R. Cristescu, A. J. Bass, K.-M. Kim, J. I. Odegaard, K. Kim, X. Q. Liu, X. Sher, H. Jung, M. Lee, S. Lee, S. H. Park, J. O. Park, Y. S. Park, H. Y. Lim, H. Lee, M. Choi, A. Talasaz, P. S. Kang, J. Cheng, A. Loboda, J. Lee, W. K. Kang, Comprehensive molecular characterization of clinical responses to PD-1 inhibition in metastatic gastric cancer. *Nat. Med.* **24**, 1449–1458 (2018).
31. M. Nurmik, P. Ullmann, F. Rodriguez, S. Haan, E. Letellier, In search of definitions: Cancer-associated fibroblasts and their markers. *Int. J. Cancer* **146**, 895–905 (2020).
32. A. Prat, A. Navarro, L. Paré, N. Reguart, P. Galván, T. Pascual, A. Martínez, P. Nuciforo, L. Comerma, L. Alos, N. Pardo, S. Cedrés, C. Fan, J. S. Parker, L. Gaba, I. Victoria, N. Viñolas, A. Vivancos, A. Arance, E. Felip, Immune-related gene expression profiling after PD-1 blockade in non–small cell lung carcinoma, head and neck squamous cell carcinoma, and melanoma. *Cancer Res.* **77**, 3540–3550 (2017).
33. M. Sade-Feldman, K. Yizhak, S. L. Bjorgaard, J. P. Ray, C. G. de Boer, R. W. Jenkins, D. J. Lieb, J. H. Chen, D. T. Frederick, M. Barzily-Rokni, S. S. Freeman, A. Reuben, P. J. Hoover, A.-C. Villani, E. Ivanova, A. Portell, P. H. Lizotte, A. R. Aref, J.-P. Eliane, M. R. Hammond, H. Vitzthum, S. M. Blackmon, B. Li, V. Gopalakrishnan, S. M. Reddy, Z. A. Cooper, C. P. Paweletz, D. A. Barbie, A. Stemmer-Rachamimov, K. T. Flaherty, J. A. Wargo, G. M. Boland, R. J. Sullivan, G. Getz, N. Hacohen, Defining t cell states associated with response to checkpoint immunotherapy in melanoma. *Cell* **175**, 998–1013.e20 (2018).
34. J.-W. Cho, M. H. Hong, S.-J. Ha, Y.-J. Kim, B. C. Cho, I. Lee, H. R. Kim, Genome-wide identification of differentially methylated promoters and enhancers associated with response to anti-PD-1 therapy in non-small cell lung cancer. *Exp. Mol. Med.* **52**, 1550–1563 (2020).
35. S. Paul, G. Lal, The molecular mechanism of natural killer cells function and its importance in cancer immunotherapy. *Front. Immunol.* **8**, 1124 (2017).
36. L. Jerby-Arnon, P. Shah, M. S. Cuoco, C. Rodman, M.-J. Su, J. C. Melms, R. Leeson, A. Kanodia, S. Mei, J.-R. Lin, S. Wang, B. Rabasha, D. Liu, G. Zhang, C. Margolais, O. Ashenberg, P. A. Ott, E. I. Buchbinder, R. Haq, F. S. Hodi, G. M. Boland, R. J. Sullivan, D. T. Frederick, B. Miao, T. Moll, K. T. Flaherty, M. Herlyn, R. W. Jenkins, R. Thummalapalli, M. S. Kowalczyk, I. Cañadas, B. Schilling, A. N. R. Cartwright, A. M. Luoma, S. Malu, P. Hwu, C. Bernatchez, M.-A. Forget, D. A. Barbie, A. K. Shalek, I. Tirosh, P. K. Sorger, K. Wucherpfennig, E. M. Van Allen, D. Schadendorf, B. E. Johnson, A. Rotem, O. Rozenblatt-Rosen, L. A. Garraway, C. H. Yoon, B. Izar, A. Regev, A cancer cell program promotes t cell exclusion and resistance to checkpoint blockade. *Cell* **175**, 984–997.e24 (2018).
37. Z. Zhang, Z.-X. Wang, Y.-X. Chen, H.-X. Wu, L. Yin, Q. Zhao, H.-Y. Luo, Z.-L. Zeng, M.-Z. Qiu, R.-H. Xu, Integrated analysis of single-cell and bulk RNA sequencing data reveals a pan-cancer stemness signature predicting immunotherapy response. *Genome Med.* **14**, 45 (2022).
38. N. A. Nicola, J. J. Babon, Leukemia inhibitory factor (LIF). *Cytokine Growth Factor Rev.* **26**, 533–544 (2015).
39. M. Pascual-García, E. Bonfill-Teixidor, E. Planas-Rigol, C. Rubio-Perez, R. Iurlaro, A. Arias, I. Cuartas, A. Sala-Hojman, L. Escudero, F. Martínez-Ricarte, I. Huber-Ruano, P. Nuciforo, L. Pedrosa, C. Marques, I. Braña, E. Garralda, M. Vieito, M. Squatrito, E. Pineda, F. Graus, C. Espejo, J. Sahuquillo, J. Tabernero, J. Seoane, LIF regulates CXCL9 in tumor-associated macrophages and prevents CD8+ T cell tumor-infiltration impairing anti-PD1 therapy. *Nat. Commun.* **10**, 2416 (2019).
40. A. Bagaev, N. Kotlov, K. Nomie, V. Svekolkin, A. Gafurov, O. Isaeva, N. Osokin, I. Kozlov, F. Frenkel, O. Gancharova, N. Almog, M. Tsiper, R. Ataullakhanov, N. Fowler, Conserved pan-cancer microenvironment subtypes predict response to immunotherapy. *Cancer Cell* **39**, 845–865.e7 (2021).
41. P. A. Ott, F. S. Hodi, H. L. Kaufman, J. M. Wigginton, J. D. Wolchok, Combination immunotherapy: A road map. *J. Immunother. Cancer* **5**, 16 (2017).
42. M. Binnewies, E. W. Roberts, K. Kersten, V. Chan, D. F. Fearon, M. Merad, L. M. Coussens, D. I. Gabrilovich, S. Ostrand-Rosenberg, C. C. Hedrick, R. H. Vonderheide, M. J. Pittet, R. K. Jain, W. Zou, T. K. Howcroft, E. C. Woodhouse, R. A. Weinberg, M. F. Krummel, Understanding the tumor immune microenvironment (TIME) for effective therapy. *Nat. Med.* **24**, 541–550 (2018).
43. K. J. Hiam-Galvez, B. M. Allen, M. H. Spitzer, Systemic immunity in cancer. *Nat. Rev. Cancer* **21**, 345–359 (2021).
44. D. Escors, M. Gato-Cañas, M. Zuazo, H. Arasanz, M. J. García-Granda, R. Vera, G. Kochan, The intracellular signalosome of PD-L1 in cancer cells. *Signal Transduct. Target. Ther.* **3**, 26 (2018).
45. S. Suresh, K. A. O'Donnell, Translational Control of Immune Evasion in Cancer. *Trends Cancer* **7**, 580–582 (2021).
46. B. A. Luca, C. B. Steen, M. Matusiak, A. Azizi, S. Varma, C. Zhu, J. Przybyl, A. Espín-Pérez, M. Diehn, A. A. Alizadeh, M. van de Rijn, A. J. Gentles, A. M. Newman, Atlas of clinically distinct cell states and ecosystems across human solid tumors. *Cell* **184**, 5482–5496.e28 (2021).

47. B. A. Helmink, S. M. Reddy, J. Gao, S. Zhang, R. Basar, R. Thakur, K. Yizhak, M. Sade-Feldman, J. Blando, G. Han, V. Gopalakrishnan, Y. Xi, H. Zhao, R. N. Amaria, H. A. Tawbi, A. P. Cogdill, W. Liu, V. S. LeBleu, F. G. Kugeratski, S. Patel, M. A. Davies, P. Hwu, J. E. Lee, J. E. Gershenwald, A. Lucci, R. Arora, S. Woodman, E. Z. Keung, P.-O. Gaudreau, A. Reuben, C. N. Spencer, E. M. Burton, L. E. Haydu, A. J. Lazar, R. Zapassodi, C. W. Hudgens, D. A. Ledesma, S. Ong, M. Bailey, S. Warren, D. Rao, O. Krijgsman, E. A. Rozeman, D. Peeper, C. U. Blank, T. N. Schumacher, L. H. Butterfield, M. A. Zelazowska, K. M. McBride, R. Kalluri, J. Allison, F. Petitprez, W. H. Fridman, C. Sautès-Fridman, N. Hacohen, K. Rezvani, P. Sharma, M. T. Tetzlaff, L. Wang, J. A. Wargo, B cells and tertiary lymphoid structures promote immunotherapy response. *Nature* **577**, 549–555 (2020).
48. R. Cabrita, M. Lauss, A. Sanna, M. Donia, M. Skaarup Larsen, S. Mitra, I. Johansson, B. Phung, K. Harbst, J. Vallon-Christersson, A. van Schoiack, K. Lövgren, S. Warren, K. Jirström, H. Olsson, K. Pietras, C. Ingvar, K. Isaksson, D. Schadendorf, H. Schmidt, L. Bastholt, A. Carneiro, J. A. Wargo, I. M. Svane, G. Jönsson, Tertiary lymphoid structures improve immunotherapy and survival in melanoma. *Nature* **577**, 561–565 (2020).
49. K. Kohli, V. G. Pillarisetty, T. S. Kim, Key chemokines direct migration of immune cells in solid tumors. *Cancer Gene Ther.* **29**, 10–21 (2022).
50. M. Zhang, W. Yang, P. Wang, Y. Deng, Y.-T. Dong, F.-F. Liu, R. Huang, P. Zhang, Y.-Q. Duan, X.-D. Liu, D. Lin, Q. Chu, B. Zhong, CCL7 recruits cDC1 to promote antitumor immunity and facilitate checkpoint immunotherapy to non-small cell lung cancer. *Nat. Commun.* **11**, 6119 (2020).
51. J. Foeng, I. Comerford, S. R. McColl, Harnessing the chemokine system to home CAR-T cells into solid tumors. *Cell Rep. Med.* **3**, 100543 (2022).
52. Y.-T. Liu, Z.-J. Sun, Turning cold tumors into hot tumors by improving T-cell infiltration. *Theranostics.* **11**, 5365–5386 (2021).
53. Y. Huang, B. Y. S. Kim, C. K. Chan, S. M. Hahn, I. L. Weissman, W. Jiang, Improving immune–vascular crosstalk for cancer immunotherapy. *Nat. Rev. Immunol.* **18**, 195–203 (2018).
54. I. G. House, P. Savas, J. Lai, A. X. Y. Chen, A. J. Oliver, Z. L. Teo, K. L. Todd, M. A. Henderson, L. Giuffrida, E. V. Petley, K. Sek, S. Mardiana, T. N. Gide, C. Quek, R. A. Scolyer, G. V. Long, J. S. Wilmott, S. Loi, P. K. Darcy, P. A. Beavis, Macrophage-derived CXCL9 and CXCL10 are required for antitumor immune responses following immune checkpoint blockade. *Clin. Cancer Res.* **26**, 487–504 (2020).
55. D. Cerezo-Wallis, M. Contreras-Alcalde, K. Troulé, X. Catena, C. Mucientes, T. G. Calvo, E. Cañón, C. Tejedo, P. C. Pennacchi, S. Hogan, P. Kölblinger, H. Tejero, A. X. Chen, N. Ibarz, O. Graña-Castro, L. Martinez, J. Muñoz, P. Ortiz-Romero, J. L. Rodriguez-Peralto, G. Gómez-López, F. Al-Shahrour, R. Rabadán, M. P. Levesque, D. Olmeda, M. S. Soengas, Midkine rewires the melanoma microenvironment toward a tolerogenic and immune-resistant state. *Nat. Med.* **26**, 1865–1877 (2020).
56. Y. Yin, T. Betsuyaku, J. R. Garbow, J. Miao, R. Govindan, D. M. Ornitz, Rapid induction of lung adenocarcinoma by Fibroblast Growth Factor 9 signaling through FGF Receptor 3. *Cancer Res.* **73**, 5730–5741 (2013).
57. S. Palakurthi, M. Kuraguchi, S. J. Zacharek, E. Zudaire, W. Huang, D. M. Bonal, J. Liu, A. Dhaneshwar, K. DePeaux, M. R. Gowaski, D. Bailey, S. N. Regan, E. Ivanova, C. Ferrante, J. M. English, A. Khosla, A. H. Beck, J. A. Rytlewski, C. Sanders, S. Laquerre, M. A. Bittinger, P. T. Kirschmeier, K. Packman, P. A. Janne, C. Moy, K.-K. Wong, R. I. Verona, M. V. Lorenzi, The combined effect of FGFR inhibition and PD-1 blockade promotes tumor-intrinsic induction of antitumor immunity. *Cancer Immunol. Res.* **7**, 1457–1471 (2019).
58. M. Kodama, Y. Kitadai, T. Sumida, M. Ohnishi, E. Ohara, M. Tanaka, K. Shinagawa, S. Tanaka, W. Yasui, K. Chayama, Expression of platelet-derived growth factor (PDGF)-B and PDGF-receptor β is associated with lymphatic metastasis in human gastric carcinoma. *Cancer Sci.* **101**, 1984–1989 (2010).
59. F. Huang, M. Wang, T. Yang, J. Cai, Q. Zhang, Z. Sun, X. Wu, X. Zhang, W. Zhu, H. Qian, W. Xu, Gastric cancer-derived MSC-secreted PDGF-DD promotes gastric cancer progression. *J. Cancer Res. Clin. Oncol.* **140**, 1835–1848 (2014).
60. N. E. Navin, The first five years of single-cell cancer genomics and beyond. *Genome Res.* **25**, 1499–1507 (2015).
61. P. Nieto, M. Elosua-Bayes, J. L. Trincado, D. Marchese, R. Massoni-Badosa, M. Salvany, A. Henriques, J. Nieto, S. Aguilar-Fernández, E. Mereu, C. Moutinho, S. Ruiz, P. Lorden, V. T. Chin, D. Kaczorowski, C.-L. Chan, R. Gallagher, A. Chou, E. Planas-Rigol, C. Rubio-Perez, I. Gut, J. M. Piulats, J. Seoane, J. E. Powell, E. Batlle, H. Heyn, A single-cell tumor immune atlas for precision oncology. *Genome Res.* **31**, 1913–1926 (2021).
62. H. Yuan, M. Yan, G. Zhang, W. Liu, C. Deng, G. Liao, L. Xu, T. Luo, H. Yan, Z. Long, A. Shi, T. Zhao, Y. Xiao, X. Li, CancerSEA: A cancer single-cell state atlas. *Nucleic Acids Res.* **47**, D900–D908 (2019).
63. A. Dobin, C. A. Davis, F. Schlesinger, J. Drenkow, C. Zaleski, S. Jha, P. Batut, M. Chaisson, T. R. Gingeras, STAR: Ultrafast universal RNA-seq aligner. *Bioinformatics* **29**, 15–21 (2013).
64. B. Li, C. N. Dewey, RSEM: Accurate transcript quantification from RNA-Seq data with or without a reference genome. *BMC Bioinformatics* **12**, 323 (2011).
65. M. D. Robinson, A. Oshlack, A scaling normalization method for differential expression analysis of RNA-seq data. *Genome Biol.* **11**, R25 (2010).
66. M. D. Robinson, D. J. McCarthy, G. K. Smyth, edgeR: A Bioconductor package for differential expression analysis of digital gene expression data. *Bioinformatics* **26**, 139–140 (2010).
67. J. S. Lee, N. U. Nair, G. Dinstag, L. Chapman, Y. Chung, K. Wang, S. Sinha, H. Cha, D. Kim, A. V. Schperberg, A. Srinivasan, V. Lazar, E. Rubin, S. Hwang, R. Berger, T. Beker, Z. Ronai, S. Hannenhalli, M. R. Gilbert, R. Kurzrock, S.-H. Lee, K. Aldape, E. Ruppin, Synthetic lethality-mediated precision oncology via the tumor transcriptome. *Cell* **184**, 2487–2502.e13 (2021).
68. H. W. Lee, W. Chung, H.-O. Lee, D. E. Jeong, A. Jo, J. E. Lim, J. H. Hong, D.-H. Nam, B. C. Jeong, S. H. Park, K.-M. Joo, W.-Y. Park, Single-cell RNA sequencing reveals the tumor microenvironment and facilitates strategic choices to circumvent treatment failure in a chemorefractory bladder cancer patient. *Genome Med.* **12**, 47 (2020).
69. N. Auslander, G. Zhang, J. S. Lee, D. T. Frederick, B. Miao, T. Moll, T. Tian, Z. Wei, S. Madan, R. J. Sullivan, G. Boland, K. Flaherty, M. Herlyn, E. Ruppin, Robust prediction of response to immune checkpoint blockade therapy in metastatic melanoma. *Nat. Med.* **24**, 1545–1549 (2018).
70. W. E. Johnson, C. Li, A. Rabinovic, Adjusting batch effects in microarray expression data using empirical Bayes methods. *Biostatistics* **8**, 118–127 (2007).
71. I. Tirosh, B. Izar, S. M. Prakadan, M. H. Wadsworth, D. Treacy, J. J. Trombetta, A. Rotem, C. Rodman, C. Lian, G. Murphy, M. Fallahi-Sichani, K. Dutton-Regester, J.-R. Lin, O. Cohen, P. Shah, D. Lu, A. S. Genshaft, T. K. Hughes, C. G. K. Ziegler, S. W. Kazer, A. Gaillard, K. E. Kolb, A.-C. Villani, C. M. Johannessen, A. Y. Andreev, E. M. Van Allen, M. Bertagnolli, P. K. Sorger, R. J. Sullivan, K. T. Flaherty, D. T. Frederick, J. Jané-Valbuena, C. H. Yoon, O. Rozenblatt-Rosen, A. K. Shalek, A. Regev, L. A. Garraway, Dissecting the multicellular ecosystem of metastatic melanoma by single-cell RNA-seq. *Science* **352**, 189–196 (2016).
72. P. E. Hughes, S. Caenepeel, L. C. Wu, Targeted Therapy and Checkpoint Immunotherapy Combinations for the Treatment of Cancer. *Trends Immunol.* **37**, 462–476 (2016).
73. H. R. Keller, X. Zhang, L. Li, H. Schaider, J. W. Wells, Overcoming resistance to targeted therapy with immunotherapy and combination therapy for metastatic melanoma. *Oncotarget* **8**, 75675–75686 (2017).
74. N. Karachaliou, M. Gonzalez-Cao, A. Sosa, J. Berenguer, J. W. P. Bracht, M. Ito, R. Rosell, The combination of checkpoint immunotherapy and targeted therapy in cancer. *Ann. Transl. Med.* **5**, 388 (2017).
75. D. S. Wishart, Y. D. Feunang, A. C. Guo, E. J. Lo, A. Marcu, J. R. Grant, T. Sajed, D. Johnson, C. Li, Z. Sayeeda, N. Assempour, I. Iynkkaran, Y. Liu, A. Maciejewski, N. Gale, A. Wilson, L. Chin, R. Cummings, D. Le, A. Pon, C. Knox, M. Wilson, DrugBank 5.0: A major update to the DrugBank database for 2018. *Nucleic Acids Res.* **46**, D1074–D1082 (2018).
76. D. Szklarczyk, A. Santos, C. von Mering, L. J. Jensen, P. Bork, M. Kuhn, STITCH 5: Augmenting protein–chemical interaction networks with tissue and affinity data. *Nucleic Acids Res.* **44**, D380–D384 (2016).
77. J. Lee, SBIlab/CCN_immunotherapy: version 1.0.1 (v1.0.1) (Zenodo); https://zenodo.org/records/10437373 (2023).

Acknowledgments

Funding: This study was supported by grants from the Korean National Research Foundation (2020R1A6A1A03047902 and 2021R1A2B5B01001903). **Author contributions:** Conceptualization and methodology: J.L., D.K., J.K., D.H., I.K., M.P., K.L., S.-H.I., and S.K. Investigation and visualization: J.L. and D.K. Supervision and writing—original draft: J.L. and S.K. Writing—review and editing: J.L., D.K., and S.K. **Competing interests:** The authors declare that they have no competing interests. **Data and materials availability:** All data used in this study are publicly available. All repository keys of the patient data, such as zenodo[https://zenodo.org/record/4661265], are listed in data S1. The signature matrix of melanoma and TR4 can be downloaded from the CIBERSORTx webpage [https://cibersortx.stanford.edu/] and the GitHub repository of Ecotyper (https://github.com/digitalcytometry/ecotyper/tree/master/utils/signature_matrices), respectively. The human PPI network was downloaded from STRING (https://string-db.org/). Original codes used for constructing CCN and predicting ICI efficacy are deposited in the GitHub repository [https://doi.org/10.5281/zenodo.10437373 (*77*)] and are publicly available as of the date of publication. All data needed to evaluate the conclusions in the paper are present in the paper and/or the Supplementary Materials.

Submitted 5 June 2023
Accepted 28 December 2023
Published 31 January 2024
10.1126/sciadv.adj0785